DEPARTMENT OF ENERGY

DOE/MC/26029--3272

DE93 009650

CATALYTIC CONVERSION OF LIGHT ALKANES

Progress Report for the Period of April 1, - June 30, 1992

BY:

JAMES E. LYONS

June 30, 1992

Work Performed Under Contract No: DE-FC21-90MC26029

FOR:

U.S. Department of Energy
Morgantown Energy Technology Center
Morgantown, West Virginia 26507

BY:

Sun Refining and Marketing Company
Marcus Hook, Pennsylvania 19061

QUARTERLY PROGRESS REPORT

APRIL 1, 1992 - JUNE 30, 1992

CATALYTIC CONVERSION OF LIGHT ALKANES

JAMES E. LYONS

SUN COMPANY

DISCLAIMER

ACKNOWLEDGEMENTS

The work contained in this report was performed by the following researchers:

Joseph Biscardi
Eva Birnbaum
Paul T. Bowden
Heng-Lon Chen
Vincent A. Durante
Paul E. Ellis Jr.
Harry B. Gray
Robert C. Hayes
Julia Hodge
Chen-Shi Huang
Maureen Hughes
Wayne A. Langdale
James E. Lyons
Bonnie Marcus
Denise Messick
Ronald A. Merrill
Floyd A. Moore
Harry K. Myers, Jr.
Douglas P. Ridge
Walter H. Seitzer
Shahid N. Shaikh
Wilbert H. Tsao
Richard W. Wagner
Robert W. Warren
Tilak P. Wijesekera

ABSTRACT

The second Quarterly Report of 1992 on the Catalytic Conversion of Light Alkanes reviews the work done between April 1, 1992 and June 31, 1992 on the Cooperative Agreement. The mission of this work is to devise a new catalyst which can be used in a simple economic process to convert the light alkanes in natural gas to oxygenate products that can either be used as clean-burning, high octane liquid fuels, as fuel components or as precursors to liquid hydrocarbon transportation fuel.

During the past quarter we have continued to design, prepare, characterize and test novel catalysts for the mild selective reaction of light hydrocarbons with air or oxygen to produce alcohols directly. These catalysts are designed to form active metal oxo (MO) species and to be uniquely active for the homolytic cleavage of the carbon-hydrogen bonds in light alkanes producing intermediates which can form alcohols. We continue to investigate three molecular environments for the active catalytic species that we are trying to generate: electron-deficient macrocycles (PHASE I), polyoxometallates (PHASE II), and regular oxidic lattices including zeolites and related structures as well as other molecular surface structures having metal oxo groups (PHASE I).

CONTRACT RESULTS TO DATE AND STATUS

Electron Deficient Macrocycles - Using computer-assisted molecular design techniques we have generated the concept that porphine macrocycles having nitro substituents on the meso-positions should be among the most highly electron deficient macrocycles yet devised. Iron complexes of these macrocycles should therefore be highly active catalysts for air-oxidation of light alkanes - perhaps even more active than the perhaloporphyrins examined to

date. For this reason we have begun an active program of nitroporphine synthesis and have made considerable progress on new and more efficient porphine synthesis, porphine nitration techniques and have generated for the first time new metallo(nitroporphine) complexes for use as alkane oxidation catalysts. Testing is underway and initial results will be reported in the next quarterly progress report.

Progress has also been made in synthesizing porphine macrocycles having the CF_3-group in the meso-position in place of the C_6F_5-group. The CF_3-group should be more electron withdrawing than the C_6F_5- group currently used, and thus catalysts should have higher molar activity. In addition, the CF_3-group is of lower molecular weight and CF_3-containing catalysts might be considerably less expensive to make and use.

Studies of gas phase electron affinity of porphryrin complexes are giving insight into the effects of halogens on the β- and meso positions of the prophryin ring. In addition effects on the iron center by β- and meso-halo groups is being determined. We are gaining an insight into how electron withdrawal from vaious points in the porphyrin macrocycle effects electrochemical and catalytic properties of these new materials. In addition, new studies from X-ray Photoelectron Spectroscopy are determining important electronic properties of these materials including charge density on the nitrogen atoms in the macrocyle.

During the past quarter we have compared catalytic and thermal oxidation of isobutane to TBA in order to better understand the oxidation process. The role of radical, peroxidic and hydroperoxidic intermediates has been assessed. tert-Butyl hydroperoxide has been implicated in the reaction mechanism and it has been shown that perhaloporphryin complexes are not only the most active light alkane oxidation catalysts known, but also provide the fastest rate of hydroperoxide conversion to alcohols ever observed. Nearly enzymatic in their rate, these reactions have considerable utility for alcohol production and may provide practical routes of interest.

Polyoxometallates - As indicated in our last quarterly report, we continue to assess the catalytic activity of oxidation-active first row transition metals including iron, in the coordination sphere of polyoxometallates that have been referred to in the past by Hill and co-workers as "inorganic porphryins". Because they are inorganic oxides, we expect them to hold up well under industrial process conditions so there is a great driving force for making catalytically active polyoxometallate materials. Because the reduction potential of iron and other metals in the framework of polyoxometallates is not high, catalytic activity is not as high as with the porphryin analogs.

During the past quarter we have made and tested polyoxometallates having a variety of central heteroatoms in order to vary the reduction potential of iron in the framework (see discussion in last quarterly report). We have found differences in activity as a function of [redacted] from a low of about 100 turnovers to a high of about 350 turnovers in the low temperature oxidation of propane to isopropyl alcohol and acetone. We are simultaneously studying the electrochemistry of these catalysts and will report any correlations between reduction potential and catalytic activity in the next quarterly report. We are also studying effects of [redacted] on activity of oxidation-active centers in polyoxoanions and will report on this work in the future.

Zeolitic Catalysts - We have shown that oxidation-active transition metal centers in the framework of zeolites catalyze the homolytic cleavage of C-H bonds, even the very unreactive ones in methane. These catalysts generate methyl radicals into the vapor space where under reaction conditions they are converted to methanol and by-products. In this report we consider in detail the fate of methyl radicals and, using kinetic modelling techniques, show the limits of methanol production under a variety of conditions which are likely to prevail in the laboratory. We conclude that a catalyst capable of cleaving C-H bonds to produce gas phase methyl racicals

will not be successful unless it possesses other features which direct the selectivity of surface processes. Low temperature surface catalysis is required, therefore we must learn first how to cleave C-H bonds at milder temperature and then how to control surface pathways to produce methanol as the major product.

Our earlier iron zeolites required temperatures in excess of 400^{o}C to activate the methane molecule. During the past quarter we have studied zeolitic catalysts which can activate methane at temperatures as low as 365^{o}C and ethane below 300 degrees. We hope by adjusting the surface redox potential to reduce methane oxidation temperature to near 300^{o}C where selective surface reactions could provide higher methanol yields.

TABLE OF CONTENTS

PAGE

TABLE OF CONTENTS (Cont'd)

PAGE

TABLE OF CONTENTS (Cont'd)

TABLE OF CONTENTS (Cont'd)

PAGE

TABLE OF CONTENTS (Cont'd)

PAGE

TABLES

PAGE

LIST OF FIGURES

PAGE

LIST OF FIGURES (Cont'd)

PAGE

LIST OF FIGURES (Cont'd)

PAGE

1.0 INTRODUCTION

We have found a family of new catalytic materials which, if successfully developed, will be effective in the conversion of light alkanes to alcohols or other oxygenates. Catalysts of this type have the potential to convert natural gas to clean-burning high octane liquid fuels directly without requiring the energy-intensive steam reforming step. In addition they also have the potential to upgrade light hydrocarbons found in natural gas to a variety of high value fuel and chemical products. In order for commerically useful processes to be developed, increases in catalytic life, reaction rate and selectivity are required. Recent progress in the experimental program geared to the further improvement of these catalysts is outlined in Sections 5 and 6.

2.0 PURPOSE

The mission of the work presented in this quarterly report is to generate novel catalytic technology which will permit the development of a simple, efficient and economical process for the direct conversion of natural gas to liquid transportation fuels. This process should be simple enough to liquify natural gas economically even at a remote reservoir site. It is a further mission of this work to find new routes from natural gas or its components to high value oxygenates by direct air-oxidation using these new catalysts.

The technical objective of the research is to design the first effective molecular catalyst for the direct air-oxidation of the hydrocarbons found in natural gas to an alcohol-rich oxidate which can either be used directly or converted into gasoline via known technology. The development of an efficient catalyst for the smooth and selective oxidation of light alkanes to alcohols will not only provide a solution to the problem of liquifying natural gas, but will create new opportunities to utilize the relatively inexpensive and abundant light alkanes for the production of a variety of valuable fuel and chemical products. Processes for converting natural gas or its components (methane, ethane, propane, and the butanes) to alcohols for use as motor fuels, fuel additives or fuel precursors will not only add a valuable alternative to crude oil but will produce a clean-burning, high octane alternative to conventional gasoline.

3.0 TECHNICAL BACKGROUND

The First Quarterly Report of 1992 for Catalytic Conversion of Light Alkanes Cooperative Agreement, Section 3.0, can be consulted for details of the technical background relating to this project.

4.0 METHODOLOGY

Details of the suprabiotic methodology to be used to conduct research on the Catalytic Conversion of Light Alkanes can be found in Section 4.0 of the First Quarterly Report of the Cooperative Agreement.

5.0 RESULTS AND DISCUSSION

The three major thrusts of the research program are catalysis by A) metals in electron deficient macrocyles (PHASE I), B) polyoxometallates (PHASE II), and C, metals in regular oxidic matrices (PHASE III).

MISSING PAGES INTENTIONALLY REMOVED

FIGURE 5-1 MASS SPECTRUM OF FePCl

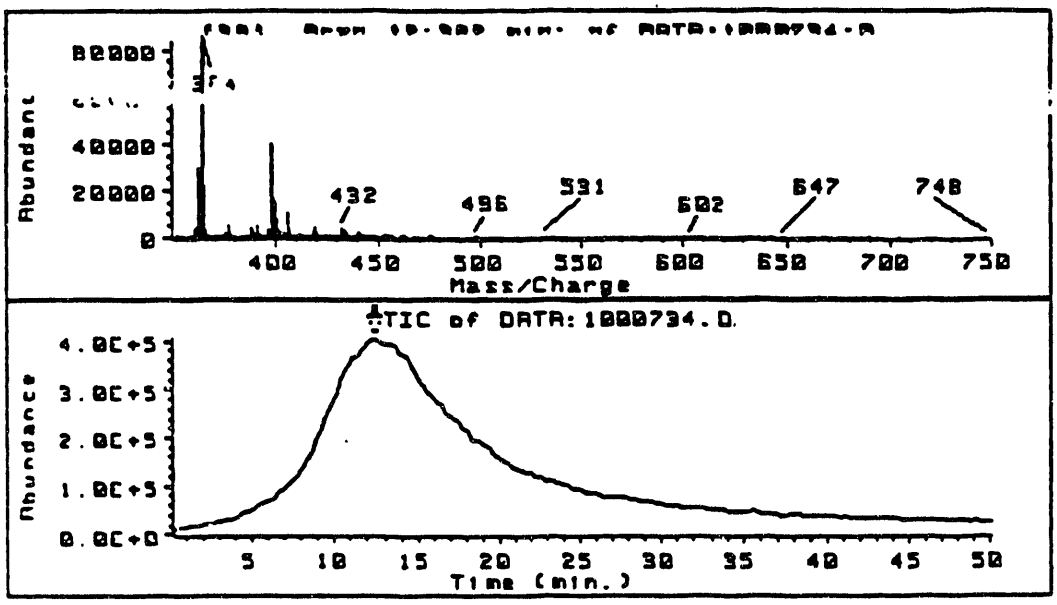

T: ----------
Z: TIC of DATA:1000734.D
Y: ----------
X: Scan 12.382 min. of DATA:1

[MS3]

Scan 12.382 min. of DATA:1000734.D

AMU.	Abundance	AMU.	Abundance	AMU.	Abundance
351.10	12.19	389.15	31.01	427.00	9.35
352.20	5.43	390.15	17.52	428.10	5.43
353.20	5.57	391.15	56.53	429.10	4.65
354.30	4.37	392.15	22.13	430.00	5.79
355.20	4.61	393.15	7.65	431.10	7.93
356.20	3.63	394.25	4.32	432.00	52.79
357.20	4.50	395.25	5.73	433.00	39.80
358.20	5.36	396.15	35.93	434.00	40.85
359.20	8.03	397.15	36.28	435.00	26.41
360.10	36.95	398.05	473.15	436.00	13.95
361.10	48.56	399.15	197.14	437.00	9.37
362.10	356.13	400.05	178.90	438.00	11.30
363.10	292.82	401.15	94.99	439.00	8.31
364.10	1000.00	402.15	39.06	440.00	34.15
365.10	259.58	403.15	34.67	441.00	24.73
366.10	36.61	404.15	31.28	442.00	16.86
367.20	7.65	405.15	22.12	443.10	11.00
368.30	4.91	406.15	127.19	444.10	4.92
369.20	6.53	407.15	37.90	445.10	5.31
370.20	4.62	408.15	8.81	446.10	5.27
371.10	8.37	409.15	5.79	447.10	5.45
372.10	8.77	410.25	4.10	448.10	9.14
373.10	13.46	411.15	18.73	449.25	5.04
374.10	13.04	411.95	15.22	450.15	3.59
375.10	30.91	412.95	12.68	451.15	3.78
376.10	16.66	413.95	10.56	452.05	8.83
377.10	63.54	415.05	9.66	453.15	14.48
378.10	31.08	416.10	8.36	454.05	13.55
[illegible]	[illegible]	417.10	[illegible]	[illegible]	[illegible]

M - CL

5.1.2.1 ZINDO Program

Since the ZINDO program in the CAChe system was used for this study, brief comments on the ZINDO program and its limitations are discussed here first.

ZINDO (Professor M.C. Zerner's Intermediate Neglect of Differential Overlap program) provides two different valence-electron-only semi-empirical procedures: a method for computing spectroscopic properties (electronic spectra) and a method of computing molecular geometries. The ZINDO program in the CAChe system is limited to 60 atoms and a maximum of 210 basis functions.

ZINDO uses the theoretically-based INDO parameterization and therefore contains parameters for transition metals. ZINDO's prediction on structures, in general, is not as reliable as MOPAC's which uses experimentally-based parameters. However, MOPAC does not deal with transition metals.

ZINDO has an alternative parameterization for electronic (UV/visible) spectra which produces good but not exact results. It is not expected that the spectra created with ZINDO will look exactly like UV-visible spectra obtained with a spectrophotometer for many reasons which will not be discussed here due to limited space.

Computational Chemistry at this level often provides only approximate results. However everything being equal, trends may be established for a given series of compounds. In this study, it was found that tetranitro-porphyrin-Cu is quite different from Zn or Fe homologs in structural shape (buckling vs. plane). To confirm the ZINDO results requires experimental study and/or higher level calculations.

5.1.2.2 Simulation Method

Compounds of porphine and its derivatives (Figure-2) were "synthesized" using the Molecular Editor program in the CAche system. Structures were initially optimized using the Molecular Mechanics program, and the optimized structures were further fine tuned using the ZINDO semi-empirical Quantum program. Based on the ZINDO outputs, a theoretical electronic spectrum of each compound was generated using the configuration interaction (CI) option with CI=14, which means that one electron is excited from any of the fourteen HOMOs into any of the fourteen LUMOs.

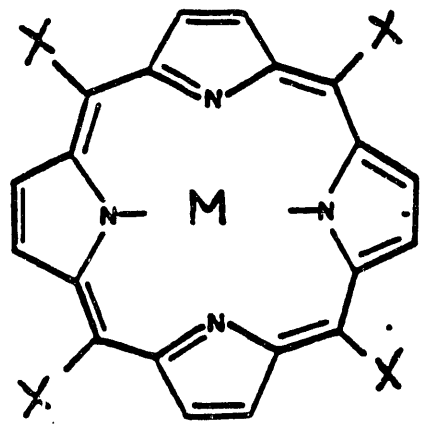

Compound	X	Metal	
I	H	H, H	P
II	NO_2	H, H	Free-base TNP
III	NO_2	Zn(+2)	TNP-Zn
IV	NO_2	Cu(+2)	TNP-Cu
V	NO_2	Fe(+2)	TNP-Fe
VI	H	Fe(+2)	Porphyrin-Fe
VII	H	Cu(+2)	Porphyrin-Cu

Note: TNP = tetranitro-porphyrin; p = porphine

FIGURE 5-2

SUBSTITUTED PORPHINE NUCLEUS

5.1.2 Conclusions

1. In most cases (except TNP-Cu), tetranitroporphinatocopper(II),the ZINDO predicts that the two oxygens of the nitro group are out of the porphyrin ring plane, suggesting that the steric problem of the nitro group could be eased by tilting the two oxygens.

2. ZINDO results indicate that metals play a key role in determining the porphyrin ring structure, e.g. buckling vs. plane.

   In the case of tetranitro-porphyrins, TNP-Cu (Figure 5-9) is buckled, TNP-Zn (Figure 5-7) much less buckled, and TNP-Fe (Figures 5-11) flat. The buckled TNP-Cu results in a shorter distance (3.658 A) between the two opposite nitrogens of porphyrin ring as shown in Table 5-1.

   TNP-Cu > TNP-Zn > TNP-Fe

   Most buckled ⟶ Flat

   In the case of porphyrins (without the nitro group), porphyrin-Cu (Figure 5-14) is slightly buckled and porphyrin-Fe (Figure 5-13, again, flat.

3. From the HOMO and LUMO energy gap listed in Table 5-2, the following trends are observed:

- The energy gap between HOMO and LUMO of metalloporphyrins is usually larger than its corresponding free base porphyrins. For example, either porphyrin-Fe (5.199 ev) or porphyrin-Cu (5.105 ev) has a larger energy gap than porphine (4.858 ev). The HOMO/LUMO energy gap of TNP-Zn (4.501 ev) or TNP-Fe (4.575 ev) is larger than tetranitroporphine (4.283 ev), but tetranitroporphyrin-Cu is (4.078 ev).

- The tetranitro groups tend to decrease the HOMO and LUMO energy gap of porphine or a given metal porphyrin system. This is illustrated with the following examples:

  porphine (4.858 ev) > free-base TNP (4.283 ev)
  Porphyrin-Fe (5.199 ev) > TNP-Fe (4.574 ev)

  Again, in the case of copper, the reverse was found, porphine-Cu (5.105 ev) vs. TNP-Cu (4.078 ev).

4. The calculated Q bands (500-600 nm) and B Bands (380-420 nm) of tetranitro-porphyrins are listed in Table III. For B bands, the wavelength decreases along the series Zn>Fe>Cu and for Q bands, Cu>Zn>Fe, note that the peak of the 694 nm band of TNP-Fe is not included.

   Again, note that the B and Q band shifts of TNP-Cu are not in the same direction.

   Nitro groups cause a red shift for both Q and B bands as illustrated in the cases of porphine vs. tetranitro-porphine, porphyrin-Fe vs. tetranitro-porphyrin-Fe, and porphyrin-Cu vs.tetranitro-porphyrin-Cu.

5. Graphic representation of HOMOs and LUMOs is not included in this report. However, each MO involved in the UV/visible absorption can be accessed when needed. It is observed that the iron centers of TNP-Fe participates in many Q and B bands but Zn and Cu do not.

5.1.2.3 Results

5.1.2.3.1 Porphine, P

The simulated porphine structure and its electronic spectra are shown in Figure 5-3 and 5-4 respectively. The tabulated absorption peaks are given below.

MOs	Energy GAPS	Peak Wavelength	Molar Absorptivity
HOMO -> LUMO	4.858 ev	661 nm	5450 l/mol-cm
HOMO -> LUMO +1	4.966	653	5450
HOMO-2 -> LUMO	7.230	364	240570
HOMO-3 -> LUMO	7.230	362	256608
HOMO-3 -> LUMO	7.251	361	256608
HOMO-2 -> LUMO	7.338	353	288684
HOMO-3 -> LUMO +1	7.359	352	288684
HOMO-2 -> LUMO +1	7.338	353	-
HOMO-1 -> LUMO	5.311	345	275684
HOMO -> LUMO +2	6.566	343	269438

5.1.2.3.2 Tetranitro-porphine, Free-Base TNP

The porphine ring of the free-base TNP is predicted to be flat with the nitro groups (actually, the two oxygens of the nitro group) out of the porphine ring (Figure 5-5). The structural information such as bond length, bond angle and dihedral angle is listed in Table 5-1.

The theoretically predicted electronic spectrum of the free-base TNP is shown in Figure 5-6. The most intensive absorption peaks and the lowest energy absorption peaks are listed below.

File Edit View Analyze Select Geometry Applications 11:46:31 AM

porphine

FIGURE 5-3

SIMULATED STRUCTURE OF PORPHINE

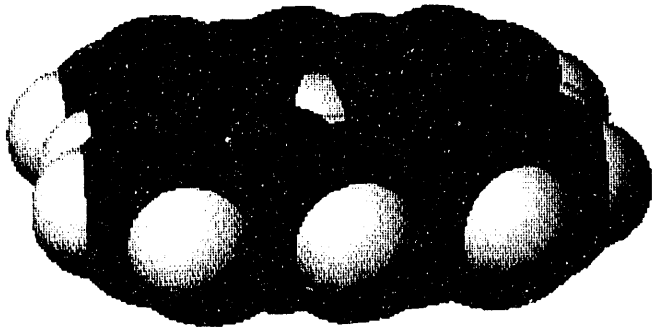

Electronic Spectra

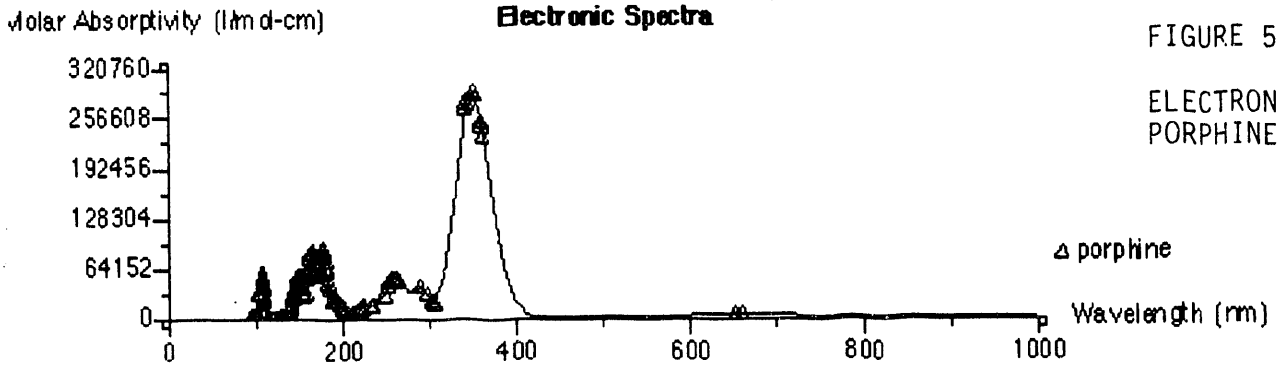

FIGURE 5-4

ELECTRONIC SPECTRUM OF PORPHINE

File Edit View Analyze Select Geometry Applications 10:16:32 AM

4nitro-porphine-mm

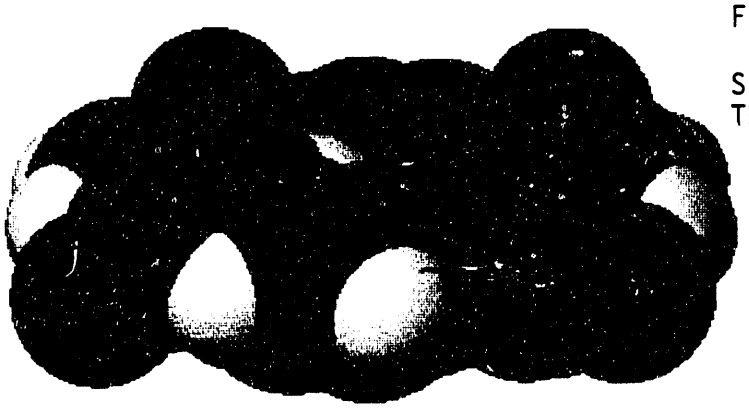

FIGURE 5-5

SIMULATED STRUCTURE OF TETRANITROPORPHINE

Electronic Spectra

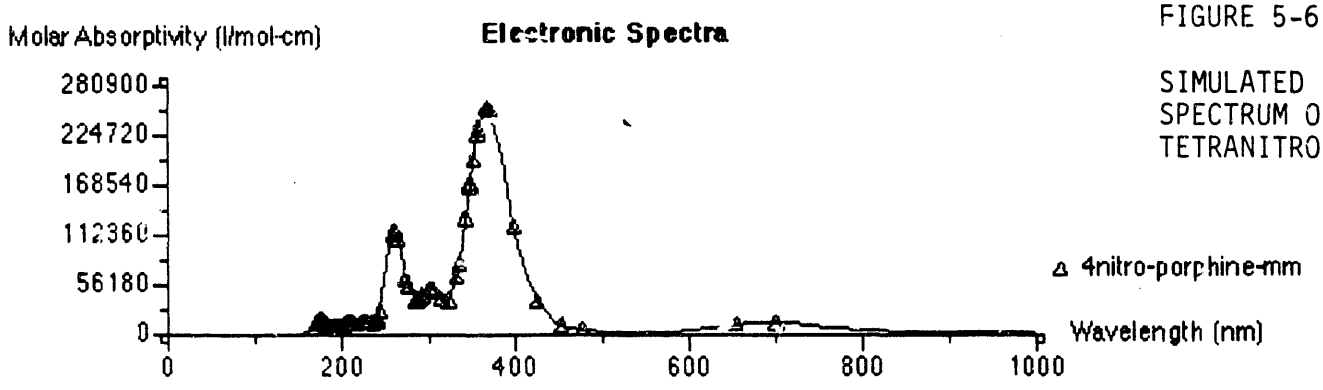

FIGURE 5-6

SIMULATED ELECTRONIC SPECTRUM OF TETRANITROPORPHINE

HOMO -> LUMO	4.283 ev.	701 nm	50 l/mol-cm
HOMO -> LUMO +1	4.525	655	50
HOMO-1 ->LUMO	5.227	369	280900
HOMO-4 -> LUMO +4	8.244	262	112360

5.1.2.3.3 Tetranitro-porphyrin-Zn, TNP-Zn

Figures 5-7 and 5-8 show the structure and electronic spectrum of TNP-Zn respectively. Some of its structural data are listed in Table 5-1. The most intensive absorption peaks and the lowest energy absorption peaks are listed below.

MOs	Energy GAPS	Peak Wavelength	Molar Absorptivity
HOMO -> LUMO	4.501 ev	656 nm	13750 l/mol-cm
HOMO -> LUMO +1	4.529	653	13750
HOMO -> LUMO +4	6.224	393	112500
HOMO -> LUMO +5	6.230	392	105750
HOMO -> LUMO +3	6.179	388	105750
HOMO-2 -> LUMO +1	7.134	357	195000
HOMO-4 -> LUMO	7.172	335	195000
HOMO-2 -> LUMO +5	8.855	193	90000

5.1.2.3.4 Tetranitro-Porphyrin-Cu, TNP-Cu

According to ZINDO calculation, TNP-Cu has a saddle shape structure (Figure 5-9). Its structural information and calculated electronic spectrum are listed in Table 5-1 and Figure 5-10 respectively. The most intensive absorption peaks and the lowest energy absorption peaks are listed below.

TABLE 5-1

STRUCTURAL DATA

	Compounds II Free Base TNP	III TNP-Zn	IV TNP-Cu	V TNP-Fe
Dihedral Angle				
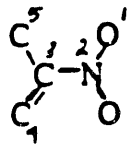				
1234	143	-152.930	-179.148	-153.264
1235	-37	28.278	1.004	28.840
Diagonal Distance				
N N	4.126	3.929	3.658	4.068
N N	4.139	3.929	3.681	4.054
Distance				
N-M		1.983	1.921	2.029
Bond Angle				
O-N-O	120.853	121.750	111.432	121.398
Bond Length				
N-O	1.232	1.231	1.211	1.232

TABLE 5-2

HOMO-LUMO Energy Gap

	HOMO	LUMO	HOMO-LUMO
Porphine	-6.341 ev	-1.483 ev	4.858 ev
Tetranitroporphine	-7.547	-3.264	4.283
Tetranitroporphyrin-Zn	-7.461	-2.960	4.501
Tetranitroporphyrin-Cu	-7.819	-3.741	4.078
Tetranitroporphyrin-Fe	-7.617	-3.042	4.575
Porphyrin-Fe	-6.448	-1.281	5.199
Porphyrin-Cu	-6.322	-1.217	5.105

TABLE 5-2a

	Q Bands (nm)	B Bands (nm)
Porphine	661,653	364,362,361
Tetranitroporphine	701,655	369
Tetranitroporphyrin-Zn	656,653	393,392,388
Tetranitroporphyrin-Cu	722	378
Tetranitroporphyrin-Fe	638,636	380,340
Porphyrin-Fe	573,572	426,421,332,323
Porphyrin-Cu	716,547,546	371,324

File Edit View Analyze Select Geometry Applications 2:32:28 PM

Tetranitro-porphyrin-Zn

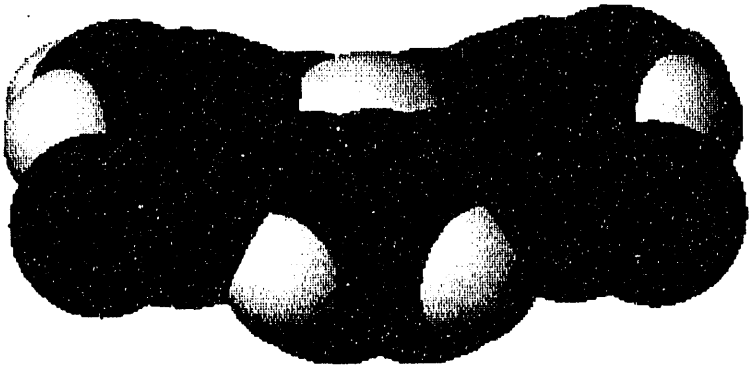

FIGURE 5-7

SIMULATED STRUCTURE OF TNP-Zn

Electronic Spectra

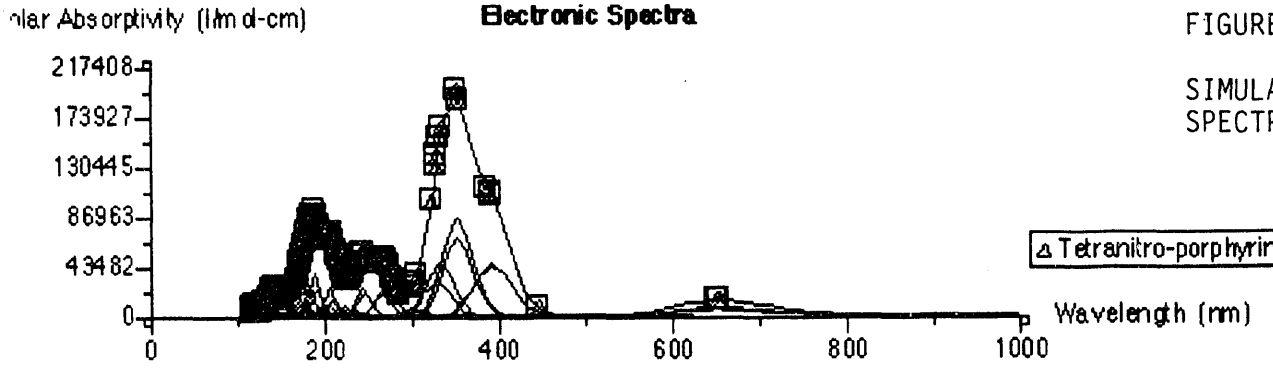

FIGURE 5-8

SIMULATED ELECTRONIC SPECTRUM OF TNP-Zn

File Edit View Analyze Select Geometry Applications 12 38 41 PM

Tetranitro-porphyrin-cu

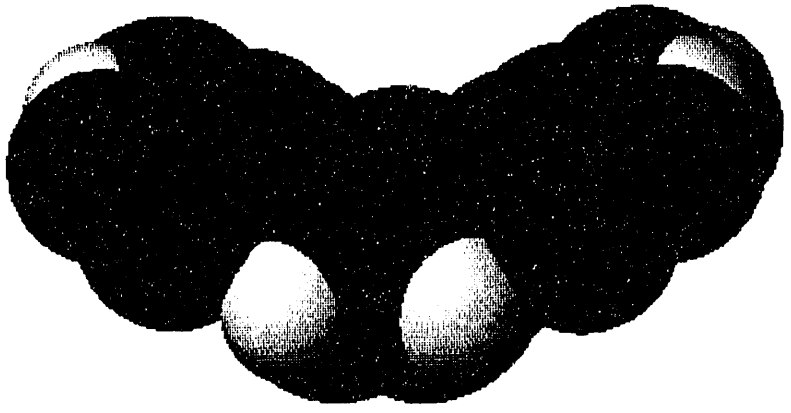

FIGURE 5-9

SIMULATED STRUCTURE OF TNP-Cu

Electronic Spectra

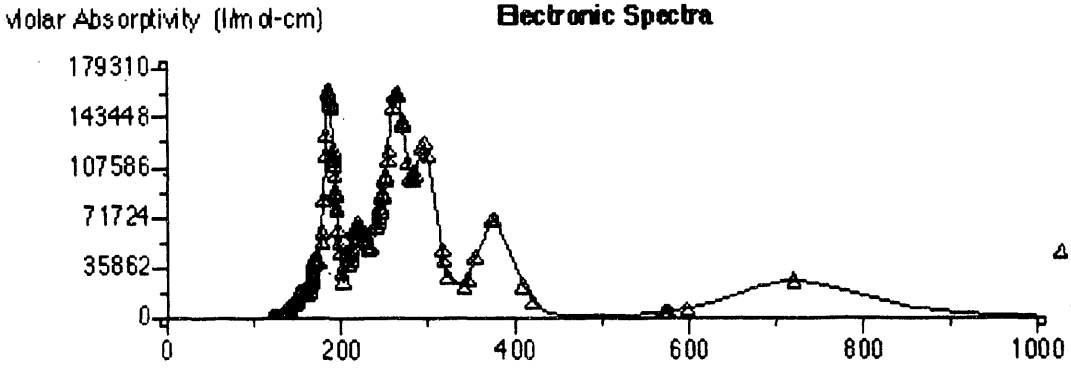

FIGURE 5-10

SIMULATED ELECTRONIC SPECTRUM OF TNP-Cu

MOs	Energy GAPS	Peak Wavelength	Molar Absorptivity
HOMO -> LUMO	4.378 EV	722 nm	26250 l/mol-cm
HOMO-1 -> LUMO	5.643	378	70000
HOMO-1 -> LUMO +2	6.400	297	133345
HOMO -> LUMO +8	7.417	268	175000
HOMO-11 -> LUMO +2	8.320	225	75000
HOMO-1 -> LUMO +10	9.084	188	170000

5.1.2.3.5 Tetranitro-porphyrin-Fe, TNP-Fe

The structure of TNP-Fe and its electronic spectrum are shown in Figure 5-11 and 5-12 respectively. Some of its structural data is listed in Table 5-1. The most intensive absorption peaks and the lowest energy absorption peaks are listed below.

MOs	Energy GAPS	Peak Wavelength	Molar Absorptivity
HOMO-8 -> LUMO +8	10.812 ev	694 nm	7800 l/mol-cm
HOMO -> LUMO	4.575	638	12000
HOMO -> LUMO +1	4.589	636	12000
HOMO-1 -> LUMO +1	5.538	380	158000
HOMO -> LUMO +5	6.380	340	183000
HOMO-3 -> LUMO +8	9.775	252	80000
HOMO-8 -> LUMO + 2	8.837	210	68900
HOMO-2 -> LUMO +9	9.725	187	190000

5.1.2.3.6 Porphyrin-Fe

A flat ring of porphyrin-Fe (Figure 5-13) is predicted by ZINDO. The most intensive and the lowest energy absorption peaks are listed below.

MOs	Energy GAPS	Peak Wavelength	Molar Absorptivity
HOMO -> LUMO	-5.167 ev	573 nm	7800 l/mol-cm
HOMO -> LUMO +1	-5.171	572	7800
HOMO-2 -> LUMO +4	10.006	426	20
HOMO-9 -> LUMO +4	11.728	421	20
HOMO-1 -> LUMO	5.629	332	350000
HOMO-1 -> LUMO +1	5.633	323	350000
HOMO-6 -> LUMO +3	6.856	320	348900
HOMO-3 -> LUMO	7.398	318	275000

File Edit View Analyze Select Geometry Applications 2:00:48 PM

Tetranitro-porphyrin-Fe

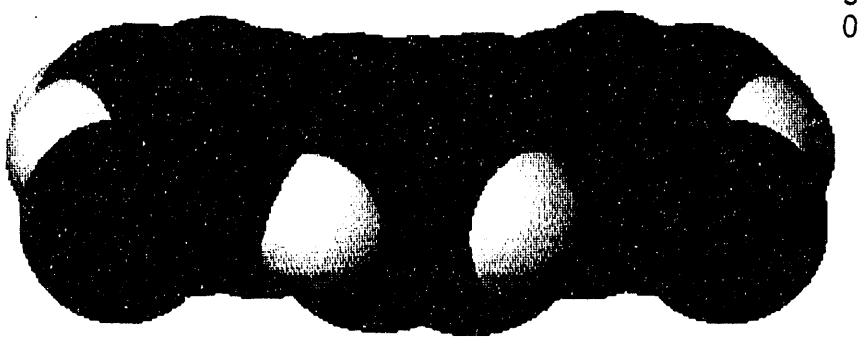

FIGURE 5-11

SIMULATED STRUCTURE OF TNP-Fe

Electronic Spectra

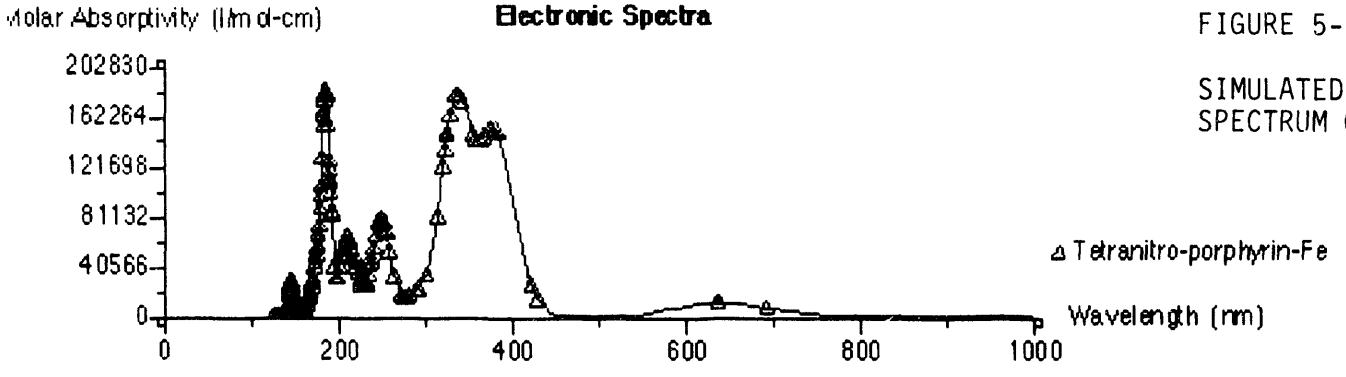

FIGURE 5-12

SIMULATED ELECTRONIC SPECTRUM OF TNP-Fe

File Edit View Analyze Select Geometry Applications 10 11 41 AM

Porphyrin-Fe

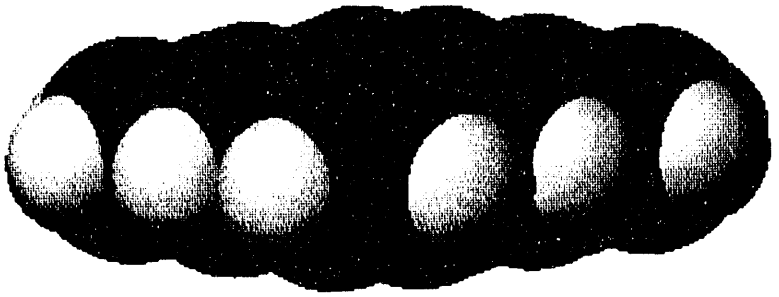

FIGURE 13

SIMULATED STRUCTURE OF FeP

Electronic Spectra

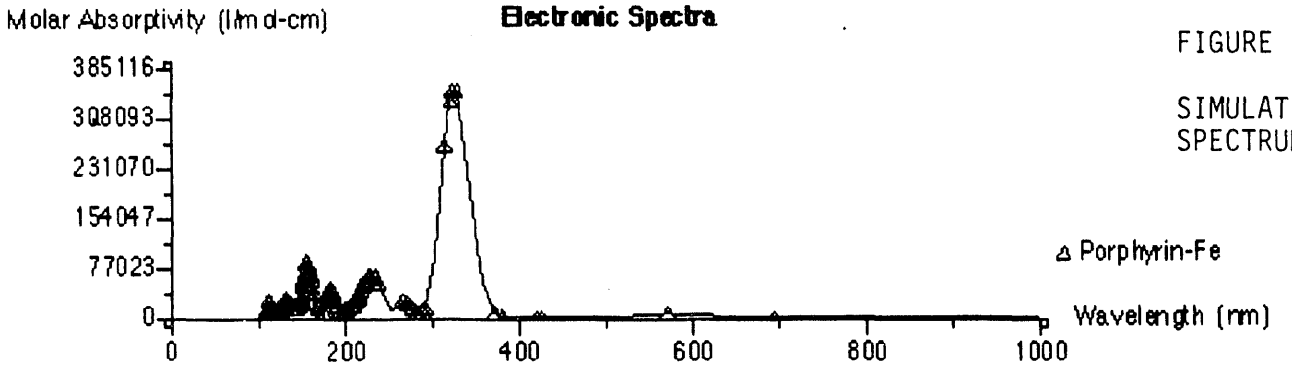

FIGURE 13a

SIMULATED ELECTRONIC SPECTRUM OF FeP

5.1.2.3.7 Porphyrin-Cu

A slightly out of plane structure (Figure 5-14) is predicted with ZINDO. The most intensive and lowest energy absorption peaks of the electronic spectra (Figure 5-15) are listed below.

MOs	Energy GAPS	Peak Wavelength	Molar Absorptivity
HOMO -> LUMO +2	5.272 ev	716 nm	50 l/mol-cm
HOMO -> LUMO +1	5.111	547	36558
HOMO -> LUMO	5.105	546	36558
HOMO-1 -> LUMO +2	6.617	371	50
HOMO -> LUMO +3	6.803	324	146233
HOMO-1 -> LUMO	6.45	319	164512

File Edit View Analyze Select Geometry Applications 11:00:53 AM

porphyrin-cu

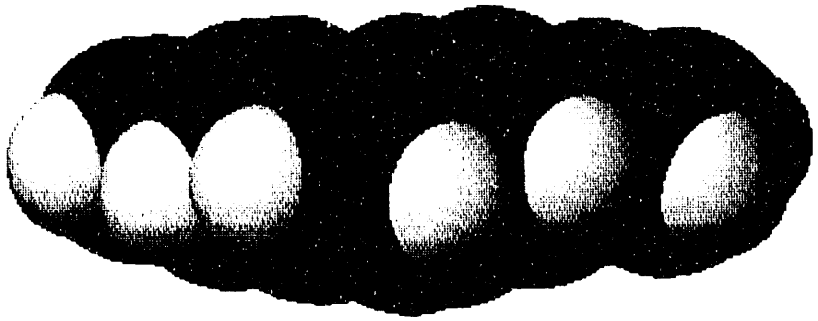

FIGURE 5-14

SIMULATED STRUCTURE OF CuP

Electronic Spectra

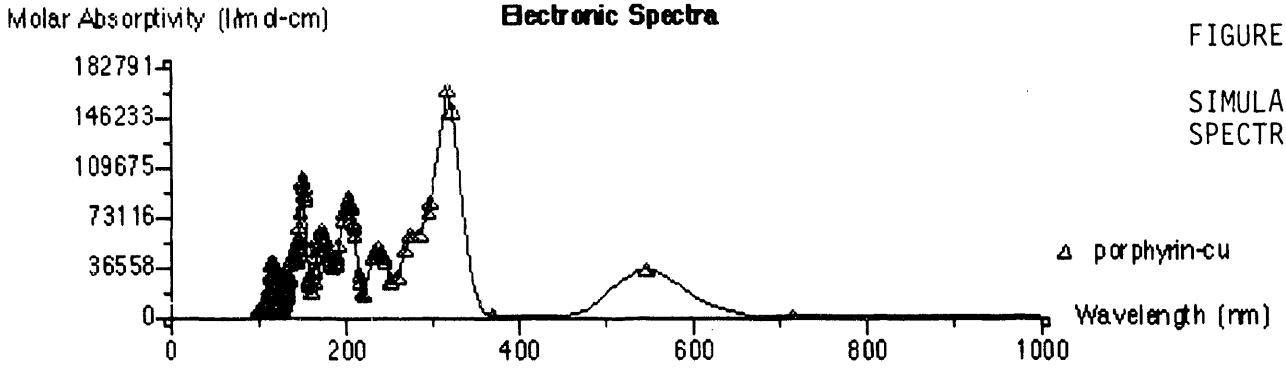

FIGURE 5-15

SIMULATED ELECTRONIC SPECTRUM OF CuP

5.1.3 PERCHLORINATED meso-TETRAPHENYLPORPHYRINS

During the past quarter, we have carried out the synthesis of Ni and Co complexes of the chlorinated meso-tetraphenylporphyrins H_2TPPCl_{20} and H_2TPPCl_{28} to be used in crystallographic and spectroscopic studies necessary to obtain structural information of the molecules. This study will help us to explain the relative effects of steric vs. electronic structures of potential oxidation catalysts.

The Ni complex of H_2TPPCl_{20} was prepared in good yield using a standard procedure and the chlorination of the peripheral pyrrolic positions carried out using chlorine gas. Spectral changes observed for both metal insertion and β-chlorination were as expected and chromatographically pure samples have been prepared. Both $NiTPPCl_{20}$ and $NiTPPCl_{28}$ were submitted for analysis by ^{252}Cf mass spectrometry.

Approximately two grams of meso-tetra(pentachlorophenyl)porphyrin (1: Figure 5-16) was prepared. One gram was purified by chromatography to be used in the metal insertion and chlorination reactions. Since the Resonance Raman and crystallographic studies required the Nickel and Cobalt complexes of the chlorinated porphyrins, it was considered appropriate to insert the metal into H_2TPPCl_{20} and attempt β-chlorination of the resulting complexes directly. Chlorinations had previously been carried out on the iron complexes since this gave the species required for catalytic studies.

Nickel insertion was carried out in DMF and $NiTPPCl_{20}$ (2: Figure 5-16) purified by filtering through a pad of neutral alumina. Metallation was found to be faster when smaller volumes were used.

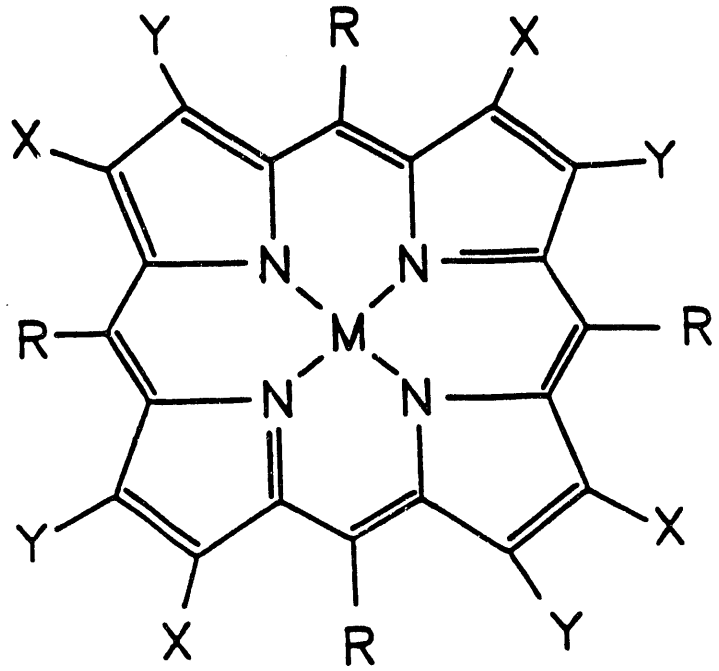

R:

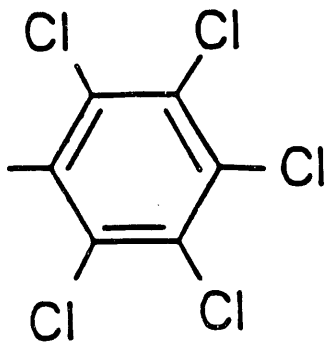

1. X = Y = H ; M = 2H

2. X = Y = H ; M = Ni

3. X = Y = Cl ; M = Ni

FIGURE 5-16

CHLORINATED METALLOTETRAPHENYL PORPHYRINS

Chlorination of the Ni complex was first attempted with N-chlorosuccinimide. $NiTPPCl_{20}$ in o-dichlorobenzene was treated with N-chlorosuccinimide and heated at 140°C. The starting material remained unchanged even after 1 h. At this stage, chlorine gas was bubbled through the solution for 3 min. and continued heating for a further 15 min. the red solution immediately turned greenish and the Soret band exhibited a red-shift of 16 nm. The two visible bands at 530 and 562 nm moved to 536, 564 and a new band appeared at 608 indicating the formation of a "chlorin" chromophore. Within 15 min. this peak increased in intensity and red-shifted to give a strong absorption at 634 nm.

The chlorination of $NiTPPCl_{20}$ was successfully effected using chlorine gas alone at 140°C. The starting material ($NiTPPCl_{20}$; red) and the product ($NiTPPCL_{28}$; 3; green) have very similar r_f values in several mixed solvent systems in addition to pure dichloromethane and benzene.

5.1.3.1 Synthesis of meso-Tetrakis(pentachlorophenyl)porphinatonickel(II), $TPPCl_{20}Ni$

meso-Tetrakis(pentachlorophenyl)porphyrin (1; 275 mg) and N,N-dimethylformamide (140 ml) were placed in a 500 ml round-bottom flask and heated to reflux with magnetic stirring. Nickel acetate tetrahydrate (1.0 g) was added and heating continued while monitoring the reaction by UV-visible spectroscopy. The 588 nm absorption of the starting material decreased with the appearance of a new peak at 562 nm. The 541 nm absorption of the starting material broadened out on the long wavelength side. The reaction was complete in 2 h. with the product showing two strong absorptions at 528 nm and 562 nm and the Soret band at 412 nm. the reaction mixture was diluted with water (300 ml), allowed to stand for 30 min. and filtered. The product was washed thoroughly with water and dried in a vacuum-dessicator.

The crude solid was dissolved in minimum chloroform, passed through dry alumina (neutral; Act. I) and eluted out cleanly with chloroform, leaving behind the impurities at the origin of the column. The pure product was obtained as a red solid by recrystallization from dichloromethane-methanol; the uv-visible spectrum is given in Figure 5-17.

5.1.3.2. Synthesis of meso-tetrakis(pentachlorophenyl)-β-octachloroporphinatonickel(II), $TPPCl_{28}Ni$

A solution of meso-Tetrakis(pentachlorophenyl)porphinatonickel(II) (NiTPPCl 20; 15 mg) in o-dichlorobenzene (8 ml) was heated to 140°C and treated with chlorine gas for 3 min. Heating was continued for 30 min. within which time the Soret band shifted from 412 nm to 436 nm. The reaction mixture was cooled to room temperature, the solvent removed under high vacuum and the product purified by passing a dichloromethane solution through neutral alumina (Act. I). The pure product was crystallized from methanol; the uv-visible spectrum is given in Figure 5-18.

5.1.4 COMPARISON OF OXIDATIONS USING $Fe(TPPF_{20}\beta\text{-}Y_8)Cl$ WITH OXIDATIONS USING $Fe(TPPCl_{20}\beta\text{-}Y_8)Cl$

It has been shown that complexes of the structure $Fe(TPPF_{20}\beta\text{-}Y_8)Cl$, Y = H(1), Cl(2), Br(3) catalyze the oxidation of alkanes using iodosyl benzene as the oxidant. In a similar manner complexes of the structure: $Fe(TPPCl_{20}\beta\text{-}Y_8)Cl$, Y = H, Cl, also catalyze the same transformations (4). On the other hand, we have recently discovered that quite surprisingly these two systems behave very differently from one another when **oxygen** is used as the oxidant. While we have demonstrated (past quarterly reports) that the complexes: $Fe(TPPF_{20}\beta\text{-}Y_8)Cl$, Y = H, Cl, Br, are exceptional catalysts (the most active known to date) for alkane oxidation using molecular oxygen, the complexes: $Fe(TPPCl_{20}\beta\text{-}Y_8)Cl$, Y = H, Cl, are **totally inactive** for oxidizing alkanes with O_2. The

---> WAVELENGTH SCAN REPORT <---

Sample Name : 999530-4
Solvent Name : CHCL3
Concentration :
Units :

Function : Absorbance
Wavelength Range : 300 to 700 nanometer
Integration Time : 1 seconds
Std Deviation : OFF

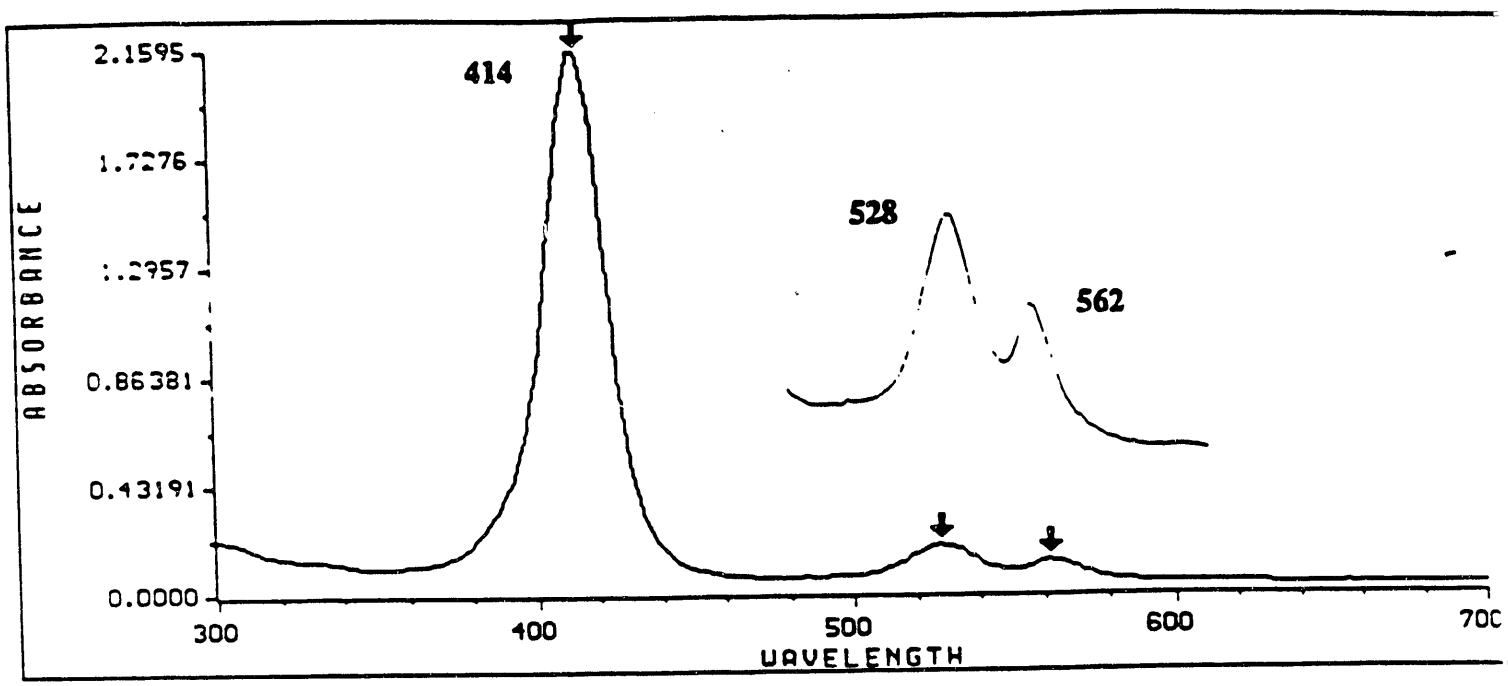

FIGURE 5-17

UV/VISIBLE SPECTRUM OF $TPPCl_{20}Ni$

---> WAVELENGTH SCAN REPORT <---

Sample Name : 996822
Solvent Name : CHCL3
Concentration : 1.0000
Units :

Function : Absorbance
Wavelength Range : 300 to 700 nanometer
Integration Time : 1 seconds
Std Deviation : OFF

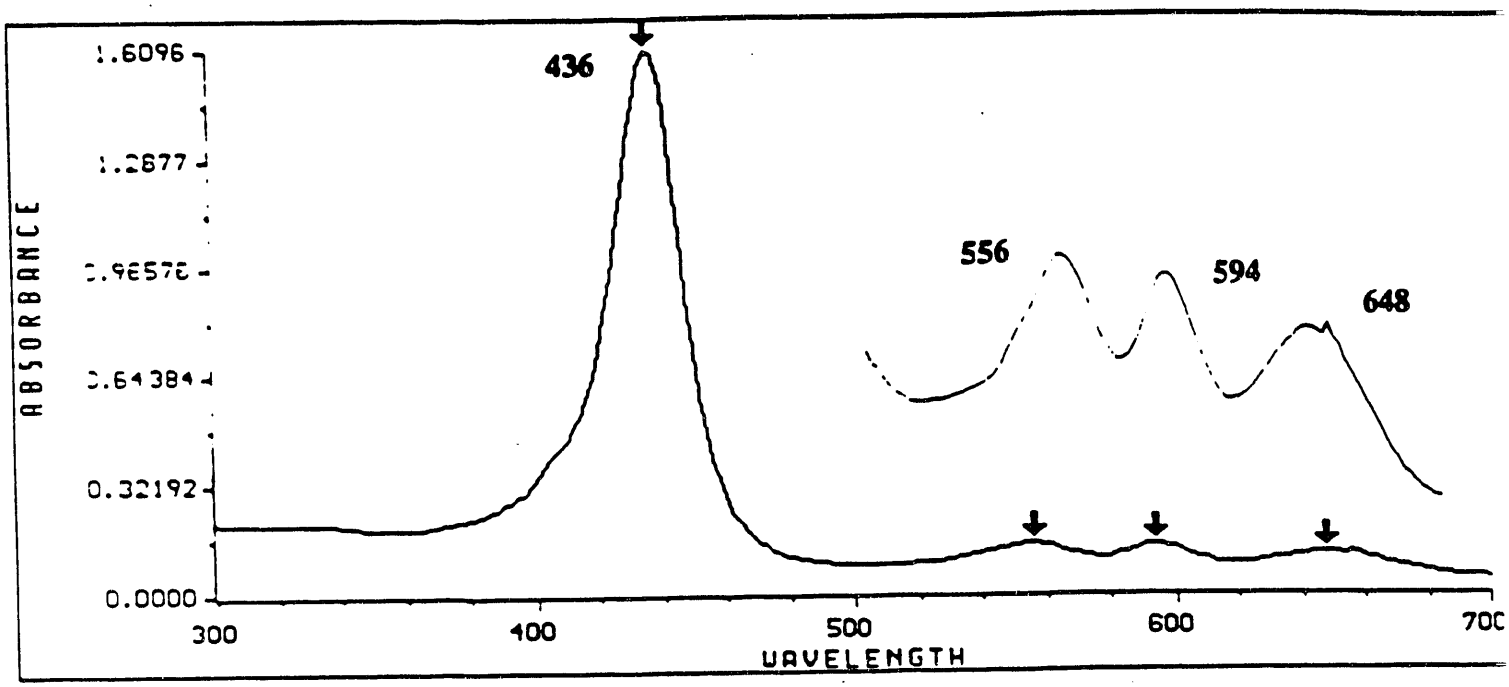

FIGURE 5-18

UV/VISIBLE SPECTRUM OF $TPPCl_{28}Ni$

complexes, Fe(TPPF$_{20}$β-Cl$_8$)Cl, and Fe(TPPCl$_{20}$β-Cl$_8$)Cl have similar Fe(III)/Fe(II) reduction potentials, E1/2 = 0.28 and 0.27 respectively (5,6). Thus they are similar electronically. Their structures, however, are not similar. The complex, Fe(TPPF$_{20}$β-Cl$_8$)Cl, is gently buckled, Figure 5-19, and the iron center is fairly well exposed. On the other hand, the complex: Fe(TPPCl$_{20}$β-Cl$_8$)Cl is very crowded with the iron center surrounded by a cluster of eight chloro groups, Figure 5-20. If the mechanism of this reaction proceeds via reductive binding of dioxygen between two iron centers, Figure 5-21, steric hindrance could prevent oxygen activation by Fe(TPPCl$_{20}$β-Cl$_8$)Cl.

References

1. M.J. Nappa and Ca.A. Tolman, Inorg. Chem., 24, 4711 (1985).

2. J.F. Bartoli, O. Brigaud, P. Battioni and D. Mansuy, Chem. Commun., 440 (1990).

3. A. Rocha Gonsolves, R. Johnstone, M. Pereira, J. Shaw and A. Sohral, Tetrahedron Letters, 32, 1355 (1991).

4. D. Dolphin, T. Kirk, R. Farrell and T. Wijesekera, World Patent WO 88/07988.

5. J. Lyons, P. Ellis, R. Wagner, P. Thompson, H. Gray, M. Hughes and J. Hodge, Petr. Div. Preprints, 37, 307 (1992).

6. T. Wijesekera, A. Matsumoto, D. Dolphin and D. Lexa. Angew. Chem. Int., Ed., 29, 1028, (1990).

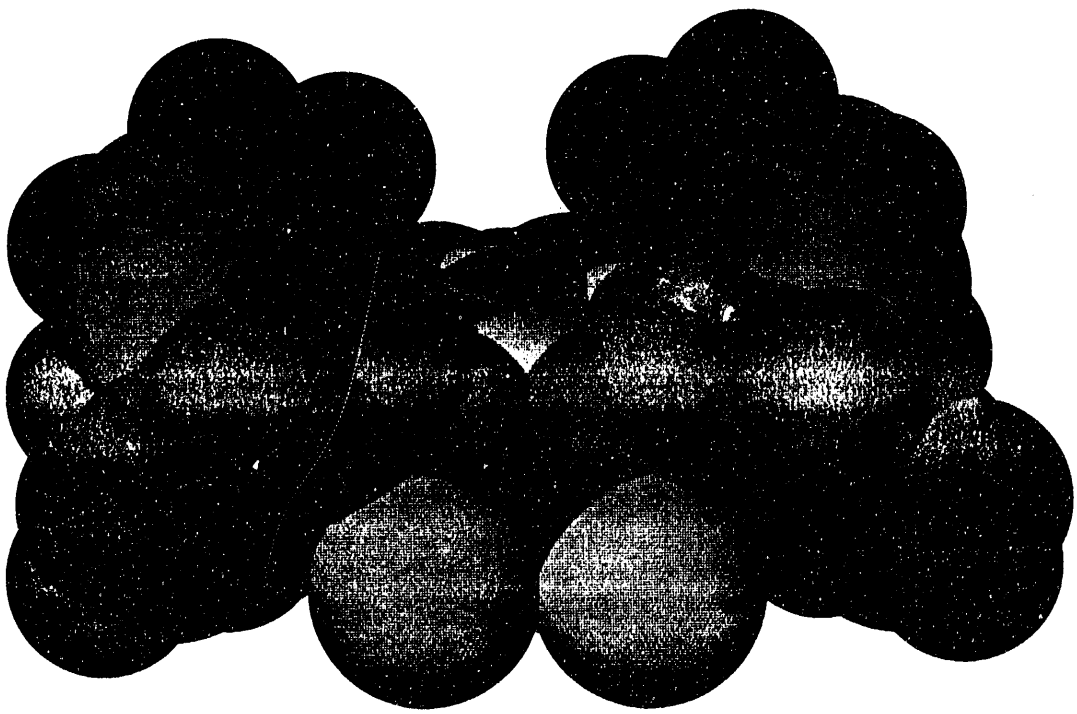

FIGURE 5-19

SIMULATED STRUCTURE OF $Fe(TPPF_{20}-Cl_8)$

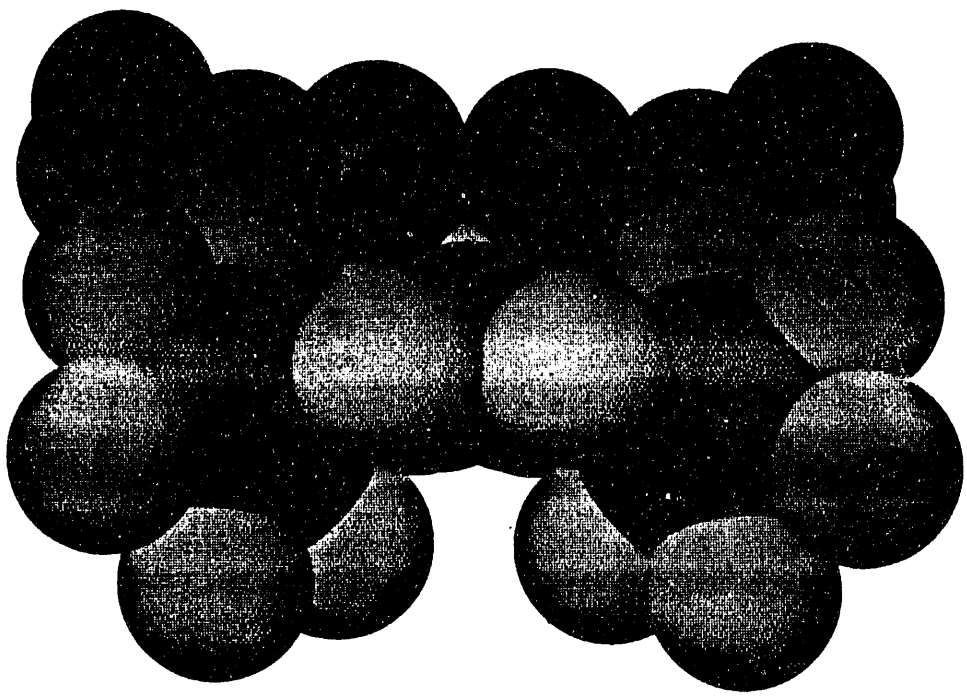

FIGURE 5-20

SIMULATED STRUCTURE OF $Fe(TPPCl_{28})$

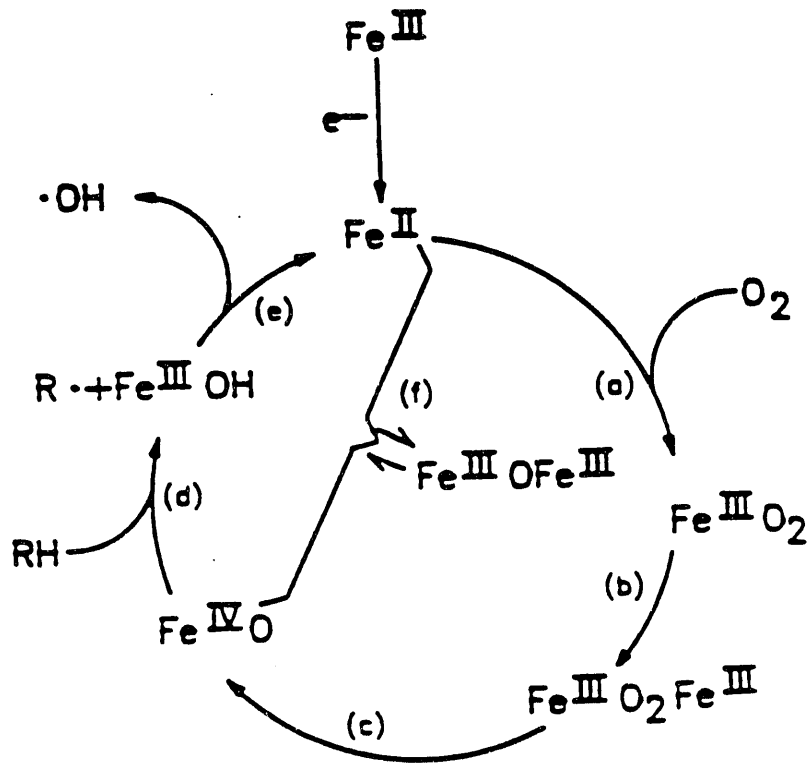

FIGURE 5-21 A Hypothetical Synthetic Dioxygenase

5.1.6 ELECTRON AFFINITY STUDIES OF IRON HALOPORPHYRIN COMPLEXES

In past quarterly reports we have described the method used to determine the electron affinity of metalloporphyrin complexes. This serves as a gas phase check on the ease of reduction of iron(III) to iron(II) and is expected to relate to both solution phase reduction potential and to catalytic activity.

Table 5-3 shows the relationships between electron affinity, reduction potential and catalytic activity for a series of iron haloporphyrin complexes. Indeed there is correspondence between electron affinity and reduction potential, and therefore to catalytic activity. We have also determined gas phase electron affinity for the complexes Fe(TPPβ-Cl_8)Cl (0.2.10ev), Fe(TPP<u>o</u>-Cl_8β-Cl_8)Cl (2.93ev), and Fe(TPPCl_{28})Cl (2.93ev), although these results are preliminary and must be refined. These numbers correspond qualitatively with reduction potentials determined by cyclic voltammetry.

---> WAVELENGTH SCAN REPORT <---

Sample Name	: 996843	Function	: Absorbance
Solvent Name	: ch2cl2	Wavelength Range	: 320 to 700 nanomet
Concentration	: 1.0000	Integration Time	: 1 seconds
Units	:	Std Deviation	: OFF

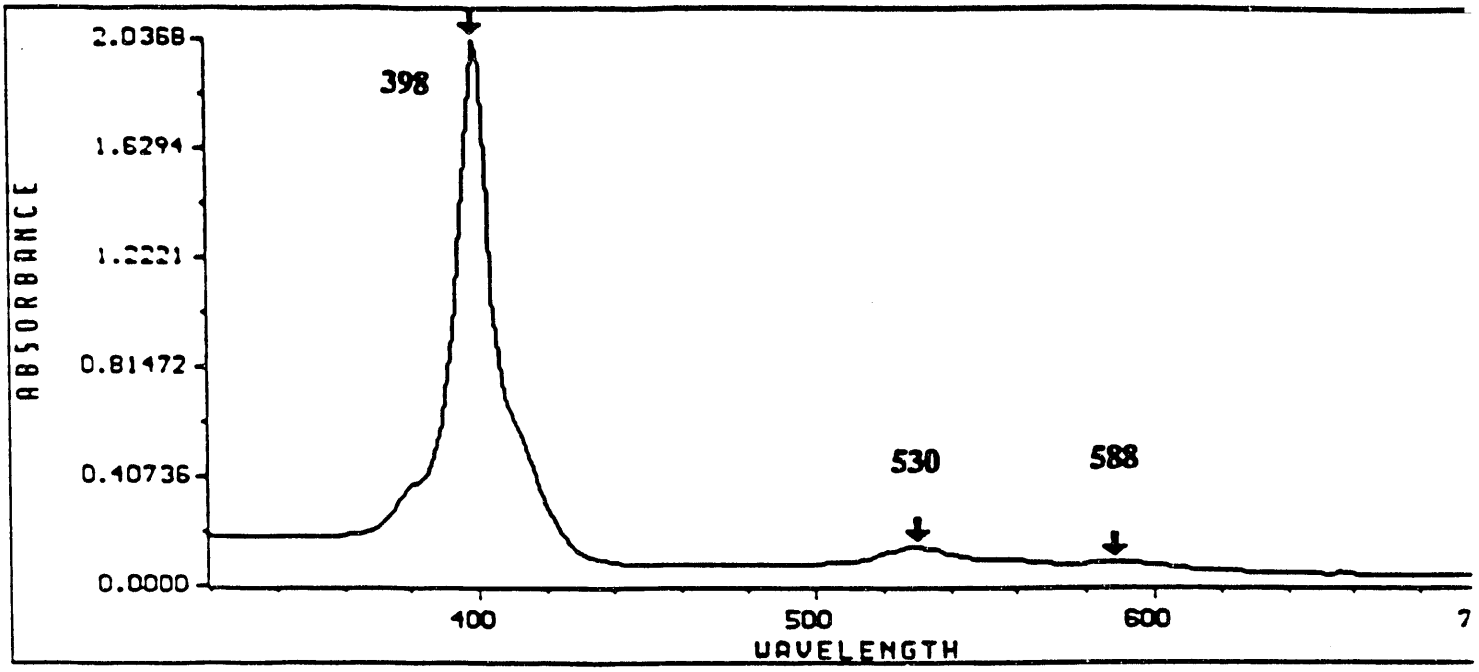

FIGURE 5-22

UV/VISIBLE SPECTRUM OF THE CYCLIZATION OF
1-TRIFLUORO-2-(2PYRROLYL)ETHYL p-NITROBENZOATE

TABLES 5-3

RELATIONSHIPS BETWEEN ELECTRON AFFINITY, REDUCTION POTENTIAL AND CATALYTIC ACTIVITY

COMPOUND	EA (ev)E	$E_{1/2}$ (ev)[a]	ACTIVITY[b]
Fe(TPP)Cl	2.15	-0.221	0
$Fe(TPPF_{20})Cl$	3.15	+0.007	1160
$Fe(TPPF_{20}\beta\text{-}Cl_8)Cl$	c	+0.28	1800

a Cyclic voltammetry in CH_2Cl_2 vs. SCE, TBAC-supporting electrolyte, glassy carbon electrode

b Catalyst turnovers for 60°C isobutane oxidations in benzene.

c This complex thermally autoreduced at 300°C during vaporization producing $Fe(II)(TPPF_{20}\beta\text{-}Cl_8)$ and Cl.

5.1.7 STUDIES OF IRON HALOPORPHYRIN COMPLEXES

The electronic structure of nitrogen in a porphyrin affects the binding ability and therefore the redox potential of the central metal in a metalloporphyrin. The electronic structure of the nitrogen can be modified by functional groups attached to the porphyrin. When tetraphenylporphyrin is modified by halogen groups, the corresponding Fe(III) porphyrins show a great improvement in light alkane oxidation activity. X-ray Photoelectron Spectrascopy (XPS) is an effective tool to differentiate the change in the electronic structure of nitrogen and/or the central metal by measuring XPS core level binding energies of nitrogen and the central metal ion (1-4). The present XPS study examines some porphyrins and iron porphyrins recently developed for the oxidation of light alkanes.

5.1.7.1 X-ray Phoelectron Spectroscopy (XPS or ESCA)

XPS studies were carried out using a Kratos Xsami surface analysis system. The system is equipped with a dual anode X-ray source (Mg and Al anode) and hemispheric analyzer. This study used only Al Ka=1486.6 eV radiation operated at 180 W (12 mA, 15 kV). The X-ray gun was set 15mm away from the sample to reduce possible damage to porphyrin samples by heat generated in the X-ray source. The base pressure in the main chamber was below $5x10^{-9}$ torr. Porphyrin samples were prepared on a gold foil in a way similar to that reported by Karweik and Winograd (5). The gold foil was then mounted on a stainless sample holder. The sample holder was then attached to a direct insertion probe which can be heated to 300°C or cooled under a liquid nitrogen flow and transferred to the main chamber for analysis. In this study the experiments were conducted at room temperature.

XPS spectra were acquired using the Kratos Vision software. Binding energy (BE) measurement was referenced to Au 4f7/2 = 84.1 eV. For N1s the BE measurements were reproduceable within +/- 0.2 eV. For Fe_2p3/2 the BE measurements were reproducible within +/- 0.2 eV. When F is present, a strong energy loss peak of the F1s line overlaps with the Fe_2p3/2 line and affects the accuracy of the Fe_2p3/2 BE measurements. In this case the measurements are reproduceable within +/- 0.5 eV. The BE results reported were an average of 2-3 measurements. We are currently negotiating with Kratos to modify the data reduction software so that the F1s energy loss line can be substracted and hence an improvement in the accuracy of Fe_2p3/2 BE measurements can be obtained. Curve fitting of the N1s spectrum was achieved using the curve fitting routine in the Kratos Vision software. The N1s spectra were resolved assuming a peak shape of 50-50 Gaussian-Lorentian combination and an equal full-width-half-maximum (FWHM) for both aza and pyrrole nitrogens in the free base porphyrins.

5.1.7.2 Materials

Tetraphenylporphyrin (H_2TPP), tetrakis(pentafluorophenyl)-porphyrin (H_2TPPF_{20}), Fe(III)TPPCl and Fe(III)$TPPF_{20}$Cl were purchased from Aldrich Chemical Co. μ-oxo-(Fe(III)TPP)$_2$O was obtained from Strem Chemicals Inc. All the above chemicals were used as received. Tetrakispentafluorophenylβ-octabromoporphyrin ($H_2TPPF_{20}Br_8$) was synthesized by Sun.

5.1.7.3 Free Base Porphyrins

Three free base porphyrins: tetraphenylporphyrin (H_2TPP), tetrakispenta-fluorophenyl)porphyrin (H_2TPPF_{20}) and tetrakis-(pentafluorophenyl)β-octabromo-porphyrin ($H_2TPPF_{20}Br_8$) were examined.

The XPS N1s spectrum of H_2TPP is shown in Figure 5-22a. The spectrum can be curve fitted into two sets of N1s lines. Each set contains a main peak and a satellite line 2.9 eV away from the main peak. The lower binding energy set (main peak=398.0 eV) is assigned to the aza nitrogen (N:) and the higher binding energy set is assigned to the pyrrole nitrogen (N:H) in the prophyrinato ring. The binding energy (BE) difference between the two main N1s peaks is 2.1 eV. The XPS N1s spectra of H_2TPPF_{20} and $H_2TPPF_{20}Br_8$ also show two sets of N peaks. The results of binding energy measurements are summarized in Table 5-4.

From Table 5-4, it is clear that modification of the porphyrinato ring with halogen groups results in an increase in the XPS N1s BE. Replacing phenyl group with pentafluorophenyl group, increases N1s BE by 0.8 eV for aza and pyrrole nitrogens. Introduction of the bromo group to the beta position of H_2TPPF_{20} results a further increase of 0.4 eV in the N1s BE. The increase in the N1s BE suggests a lower electron density of nitrogen in the halogen modified porphyrins than H_2TPP. The lower electron density can be attributed to the strong electron withdrawing properties of F and Br.

Hollander and Shirley(6) have compared the correlation of N1s BEs with atomic charges calculated by (a) CNDO (b) an extended Huckel method and (c) Pauling valence bond method. They concluded that the range of CNDO charges were the most plausible and resulted in the following equation:

$$\Delta E/\Delta Q = 10\ eV$$

Where Δ E is the BE shift in eV and Δ Q is the change in the electron density. Fadley et. al. (7) and Siegbahn et. al. (8) have shown that the relation between core level BE shift and the valence electron density change can be extended to all elements. Based on the above equation suggested by Hollander and Shirley, the results of N1s BE measurements indicate that the addition of a H+ to N reduced electronic charge by 0.21 electron. Modification of the porphyrin by repacing the 20 phenyl H's by 20 F atoms in the four phenyl rings reduces electronic charge of N by 0.08 electron. Further modification of H_2TPPF_{20} with 8 bromo groups in the beta position reduces 0.04 electron from each N.

TABLE 5-4

RESULTS OF XPS BINDING ENERGY MEASUREMENTS

	BINDING ENERGY (eV)			
	N1s		$Fe_2p3/2$	
Sample	Aza N	pyrrole N	Metallo N	
H_2TPP	398.0	400.1		
H_2TPPF_{20}	398.8	400.9		
$H_2TPPF_{20}Br$	399.2	401.3		
Fe(III)TPPCl	-		399.0	711.6
$FeTPPF_{20}$	-	399.4	713.2	
$(Fe(III)TPP)_2O$	-		398.2	710.4

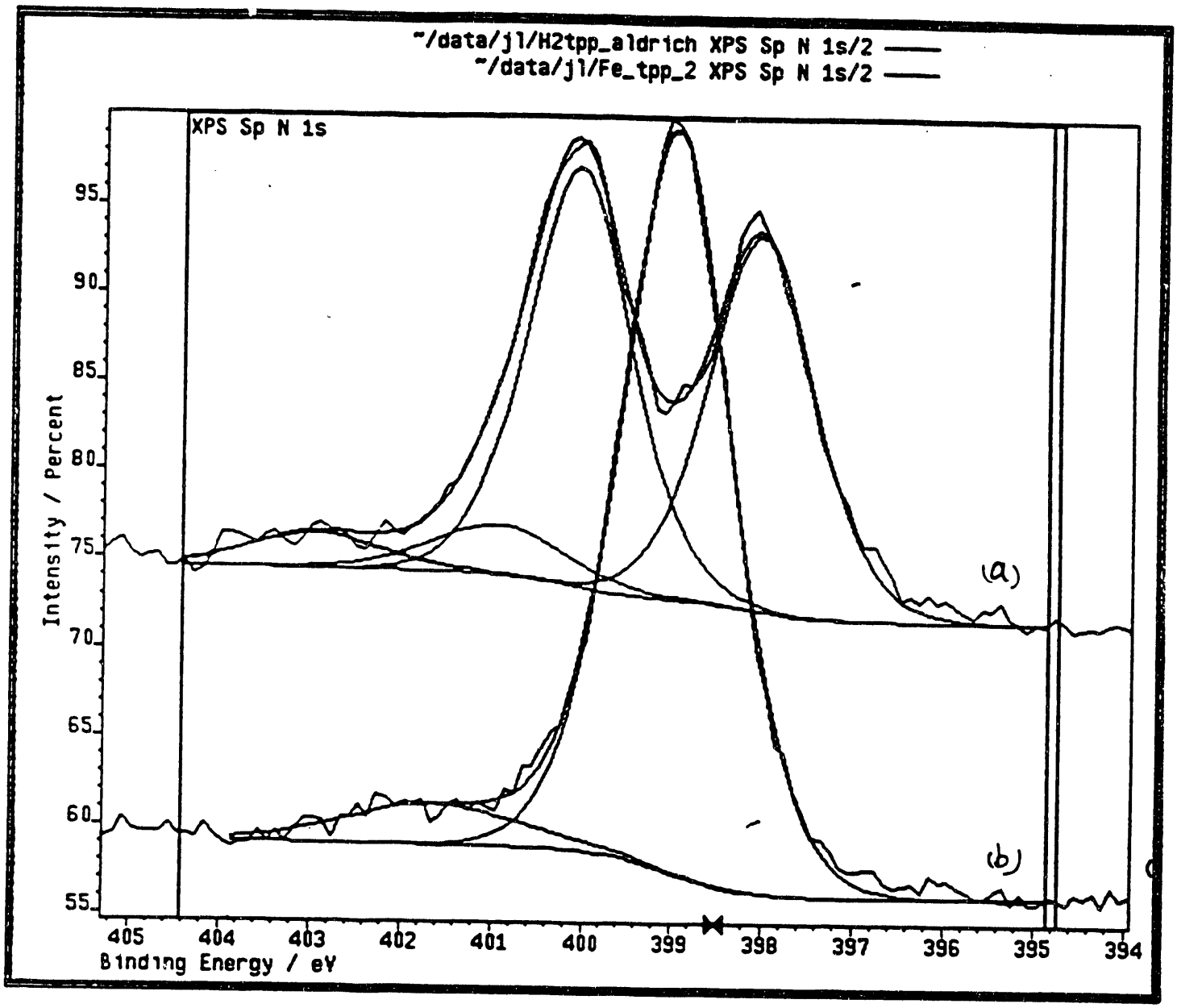

FIGURE 5-22a XPS SPECTRUM OF H_2TPP

FIGURE 5-22b XPS SPECTRUM OF Fe(TPP)Cl

5.1.7.4 Iron Porphyrins

Three iron porphyrins were examined; Fe(III)TPPCl, μ-oxo-$(Fe(III)TPP)_2O$ and $Fe(III)TPPF_{20}$.

Figure 5-22b shows the XPS N1s spectrum of Fe(III)TPPCl. Only one set of N1s main peak (BE= 399.0 eV) with a shake satellite was observed. Similar N1s spectrum was observed for the other two iron porphyrins. The observation of only one set of N 1s peaks indicates that Fe(III) bonds equally to four nitrogens in the porphyrin. The N1s BEs of those iron porphyrins are summarized in Table 5-4.

The N1s BEs of Fe(III)TPPCl and μ-oxo-$(FeTPP)_2O$ are 0.9 and 0.2 eV higher than the aza N of H_2TPP respectively. The N 1s BE of $Fe(III)TPPF_{20}$ is 0.7 eV higher than that of the aza N of H_2TPPF_{20}. The results indicate that although the Fe of μ-oxo-$(FeTPP)_2O$ is in the 3+ state, it does not modify the electron density of N as extensively as the Fe^{3+} in FeTPP or $FeTPPF_{20}$. The results also indicate that the effect of Fe^{3+} ions on the N1s electron density is stronger for FeTPP than $FeTPPF_{20}$(1.0 vs 0.6 eV).

Figure 5-23 shows the XPS Fe_2p spectra of Fe(III)TPPCl (2a), $Fe(III)TPPF_{20}Cl$ (2b) and μ-oxo-$(FeTPP)_2O$ (2c). The $Fe_2p3/2$ BEs of the iron porphyrins, measured from peak maximum, are also listed in Table 5-4. $FeTPPF_{20}Cl$ shows the highest $Fe_2p3/2$ BE and $(FeTPP)_2O$ shows the lowest $Fe_2p3/2$ BE. Comparing FeTPPCl with $(FeTPP)_2O$, it seems that the higher the $Fe_2p3/2$ BE the higher is the N1s BE. However, Kadish et. al. studied a series of Fe(III)TPPX where X = Cl, Br, ClO_4 or N_3(1). They observed that $Fe_2p3/2$ binding energies have little effect on N 1s BE. Their $Fe_2p3/2$ BEs for FeTPPCl and $(FeTPP)_2O$ are similar to our results. They, however, only observed a 0.2 eV (vs 0.8 eV in this study) difference in N1s BEs between FeTPPCl and $(FeTPP)_2O$. The reason for this inconsistency between their and our results is not clear at this moment.

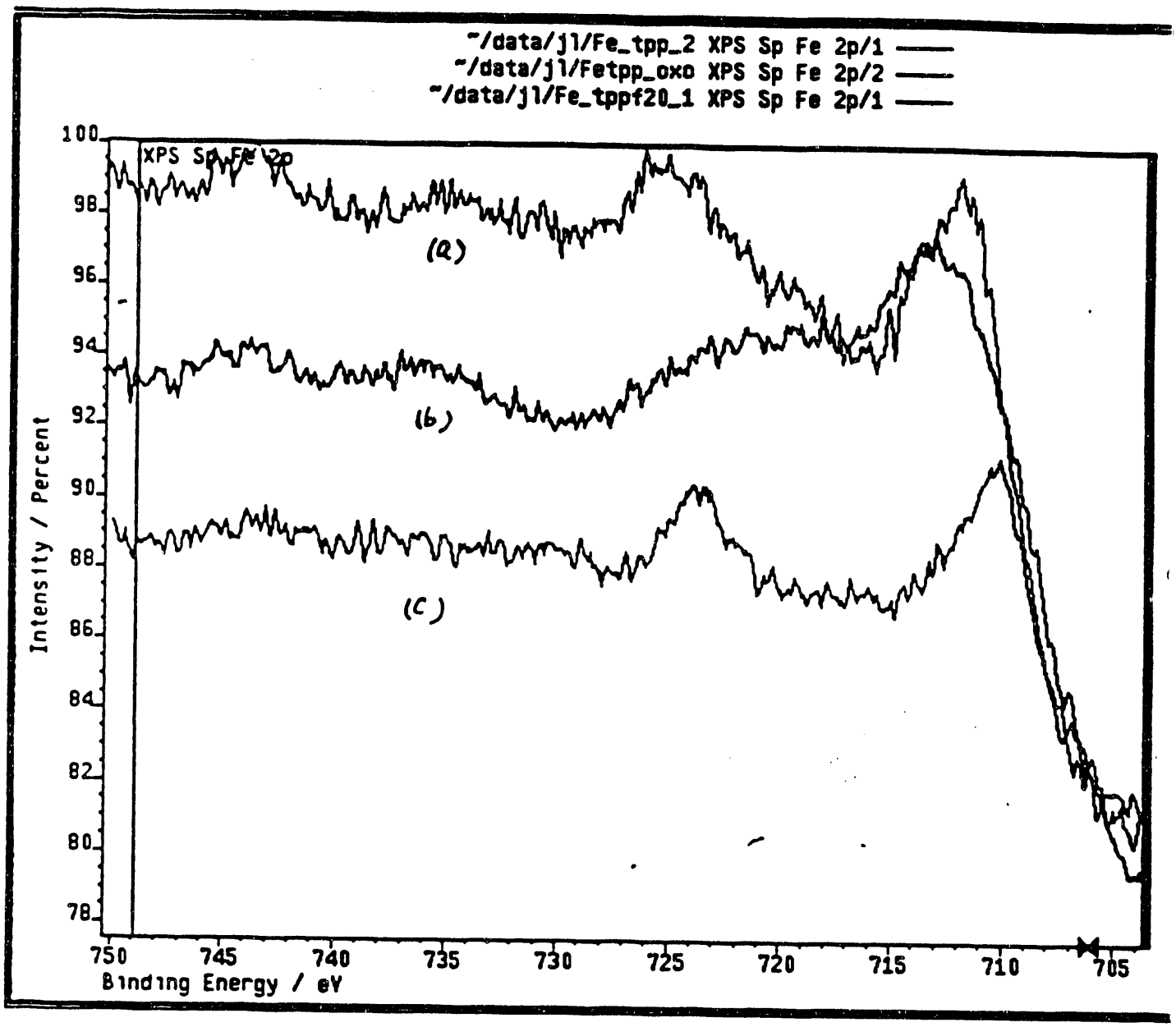

FIGURE 5-23

XPS Fe_2p SPECTRA OF Fe(III)TPPCl(a),Fe(III)

$TPPF_{20}Cl$(b), AND OXO-$(FeTPP)_2O$(c)

Kadish et. al. have also correlated XPS $Fe_2p3/2$ BEs with half-wave potentials for reduction of Fe(III) to Fe(II) for a series of Fe(III)TPPX and FeOEP(III)X where X=ClO_4, Cl, Br or N_3(1). They found a linear relationship between $Fe_2p3/2$ BEs and the half-wave potentials. Their results are reproduced in Figure 5-24 (open circles). When our data for Fe(III)TPPCl and Fe(III)$TPPF_{20}$Cl are included into Figure 5-24 (filled circles), the trend remains. Thus the relationship between $Fe_2p3/2$ BE and half-wave potential for reduction of Fe(III) to Fe(II) seems also to apply to Fe(III)TPPCl and Fe(III)$TPPF_{20}$.

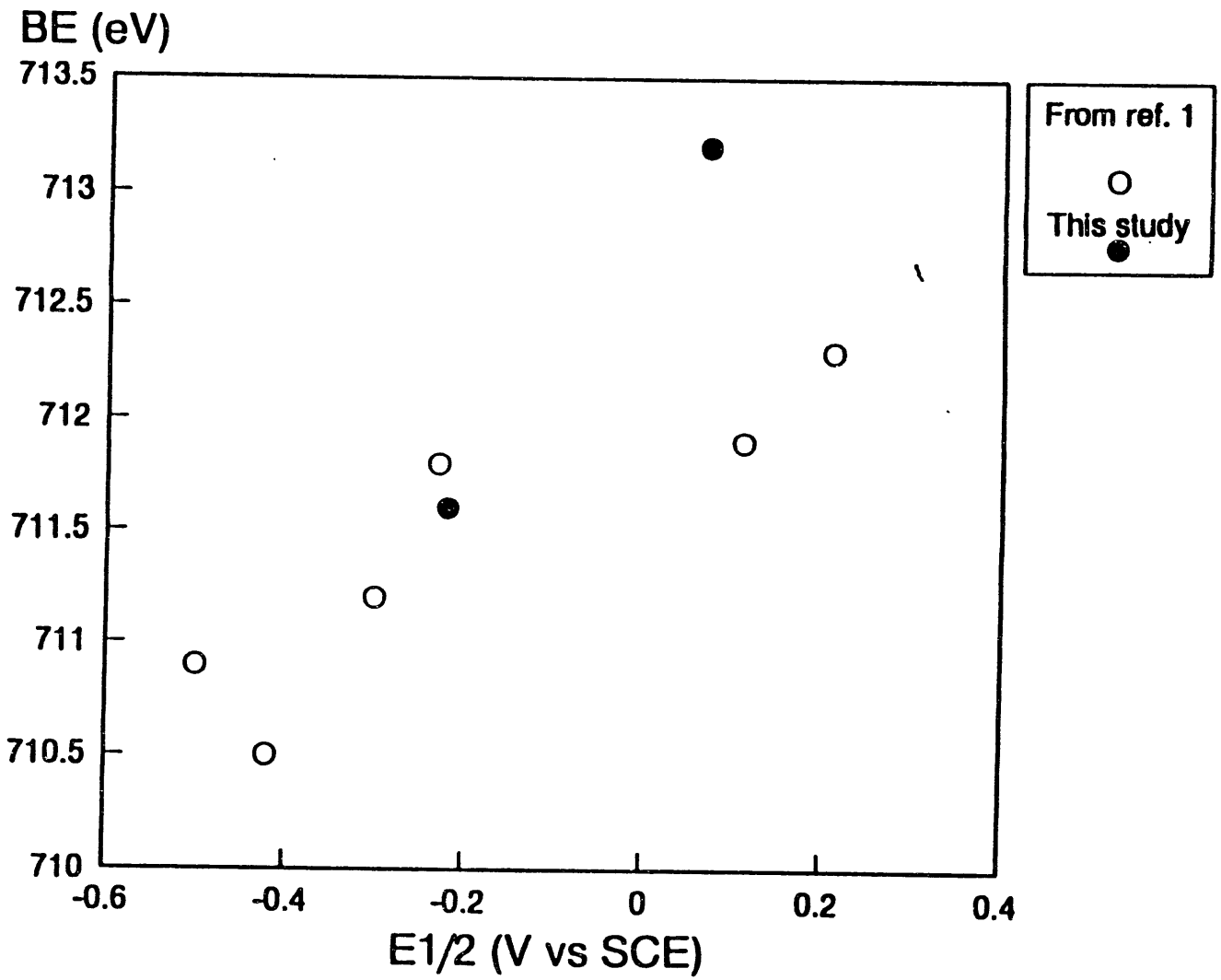

FIGURE 5-24

XPS $Fe_2p3/2$ BE VS. Fe(III)/Fe(II)
REDUCTION POTENTIAL

5.1.7.5 References

1. K.M. Kadish, L.Bottomley, J.G. Brace and N. Winograd, JACS, 102 4341 (1980)

2. Y. Niwa, H. Kobayashi and T. Tsuchiya, JACS, 60 799 (1974)

3. J.P. Macquet, M.M. Millard and T. Theophanides, JACS, 100 4741 (1978)

4. E.G. Ferrer and E.J. Baran, J. Electron Spectrosc. Relat. Phenomena, 57 189 (1991)

5. D.H. Karweik and N. Winograd, Inorg. Chem. 15 2336 (1976)

6. J.M. Hollander and D. A. Shirley, Ann. Rev. Nucl. Sci., 20 435 (1970)

7. C.S. Fadley, S.B.M. Hagstrom, M.P. Klein and D. A. Shirley, J. Chem. Phys. 48, 2779 (1968)

8. K. Siegbahn, C. Nordling, A.Fahlman, R. Nordberg, K. Hamrin, J.Hedman, G. Johanson, T. Bergmark, S. Karlsson, I. Lindgren and B. Lindberg, Nova Acta Refiae Soc. Sci., Upsaliemsis Ser. IV, Vol 20 1967.

5.1.8 ELECTRONIC SPECTROSCOPY OF HALOPORPHYRIN COMPLEXES

5.1.8.1 UV/Visible Spectroscopy of M(II)($TPPF_{20}\beta$-Y_8)

We have proposed that constant regeneration of Fe(II) during oxidation due to high Fe(III)/Fe(II) reduction potentials is the key to active alkane oxidation catalysts. Although Fe(II) complexes may not be air stable and therefore inconvenient to analyze spectoscopically, many stable metal(II) porphyrin complexes exist and their UV/Visible spectra have now been recorded. Table 5-5 lists the positions of the Soret bands for the complexes M(II)($TPPF_{20}\beta$-Cl_8)Cl and M(II)($TPPF_{20}\beta$-Br_8)Cl. For first row group VIII transition metals, Soret absorptions between 428 and 439 nm are observed.

5.1.8.2 X-Ray Crystal Structure Determination of M(II)($TPPF_{20}\beta$-Y_8)

We have now determined the structures of a number of perhalogenated porphryins and metalloporphyrins. Several of these structures have been shown in previous quarterly reports. The buckling of these complexes has been noted and the effect of buckling on catalytic activity discussed. Table 5-6 summarizes the crystal strucure data gathered which indicate the degree of distortion from planarity of the atoms in the porphryin ring.

5.1.8.3 Electronic Structure of Halogenated Metalloporphryins

The absorption bands of a series of halogenated porphyrins shift to lower energies as the size of the porphyrin substituents increases. AM1 calculations show that the red shifting in the absorption spectrum is due to a decrease in the HOMO-LUMO energy gap, which is a result of the distortion of the porphyrin ring. As we pointed out in the last quarterly report, the electronic effect of the halogens is to lower the absolute energies of the orbitals. During the past quarter geometry optimizations were improved to increase the accuracy of the calculations. As a result, the geometries became less distorted causing a decrease in the transition energies, Table 5-7. At this point, $TPPF_{20}\beta$-Cl_8 and $TPPF_{20}\beta$-Br_8 are available in their final geometries.

TABLE 5-5

Soret Positions

Chlorinated Porphyrins [a]

Metal	Soret λ
Palladium	423
Cobalt	428
Copper	430
Nickel	439
Zinc	440
Silver	494

Brominated Porphyrins [b]

Metal	Soret λ
Palladium	431
Copper	436
Nickel	433
Zinc	466
Silver	508

[a] $M(TPPF_{20}\beta\text{-}Cl_8)$

[b] $M(TPPF_{20}\beta\text{-}Br_8)$

TABLE 5-6

Crystal Structure Data:

Distortion (Å from plane of porphyrin)	$CuCl_8$	$NiBr_8$	$CuBr_8$	H_2Br_8	$ZnBr_8$
C_{meso}-	±0.128	±0.211	±0.177	±0.091	±0.021
Cβ-	±0.797	±1.326	±1.247	±0.903	±0.971
N	±0.12	±0.19	±0.15	±0.076	±0.082
Cl or Br	±1.19	±2.05	±1.99	±1.72	±1.68
'Core Size' Ct---N	2.007	1.902	1.969		2.042

5.1.9 MECHANISMS OF ISOBUTANE OXIDATION

In an effort to further understand the mode of operation of the perhaloporphyrin complexes in catalyzing the oxidation of isobutane to tert-butyl alcohol, TBA, we have considered that a possible pathway may involve the catalytic generation of radicals at low temperatures. Under very mild conditions radical reactions may give rise to selective oxidation processes. In this regard we have compared the thermal oxidation of isobutane with that of catalytic oxidation in an attempt to gain further insight into these reactions.

5.1.9.1 Thermal Oxidation of Isobutane

Overall, the thermal reaction rate is independent of oxygen pressure but proportional to the square of the isobutane concentration (carbon tetrachloride solvent). The only active hydrogen is the tertiary hydrogen, so initiation gives the tert-butyl radical, t-Bu•. The following reactions form the chain:

(1)	t-Bu• + O_2	⟶ t-BuOO]•	A fast reaction
(2)	t-BuOO• + i-BuH	⟶ t-BuOOH + t-Bu•	Hydroperoxide is ~1/2 the product
(3)	t-BuOO• + t-BuOO•	⟶ 2t-BuO• + O_2	
(4)	t-BuO• + i-BuH	⟶ t-BuOH + t-Bu•	Alcohol is ~1/2 the product
(5)	t-BuO•	⟶ Acetone + CH3•	~ 2% of the product at 145°C

TABLE 5-7

Porphyrin Calculations

Absorption data

Compound	Q_x	Q_y	Soret
$TFPPCl_8$	624 nm	536 nm	436 nm
$TFPPBr_8$	640 nm	553 nm	452 nm

Calculated data

Compound	Q_x	Q_y	Soret $_x$	Soret$_y$
$TFPPCl_8$	513 nm	506 nm	342 nm	340 nm
$TFPPBr_8$	558 nm	533 nm	354 nm	350 nm

Orbital Energies

	b_1	b_2	c_1	c_2
$TFPPCl_8$	-9.07	-9.08	-2.77	-2.57
$TFPPBr_8$	-8.97	-9.03	-2.92	-2.90

Before escaping the cage at 50-100°C, about 10% of the t-BuO• reacts with itself to form di-tert-butylperoxide which is fairly stable at this temperature.

5.1.9.2 Catalytic Oxidations

Thermal oxidations require elevated temperatures whereas iron perhaloporphyrin complexes catalyze reactions as low as room temperature and are highly active for isobutane oxidation at 60°C. One possible way in which these complexes may operate as catalysts is shown in Figure 5-25. If R• and HO• combine in the coordination sphere to expel ROH, this scheme can be regarded as a catalytic cycle in which the iron is a true catalyst. If, however, the bound radical product of equation (d) escapes into the medium, it would undergo radical reactions the same as those shown in the thermal pathway above. The iron complex then should be more proprerly regarded as a living initiator rather than as a true catalyst. If this is so, the 'catalytic' pathway should be as follows:

		Catalyst
Initiation:	(1)	$2RH + 0.5O_2$ ----------> $2R\bullet + H2O$
Chain:	(2)	$R\bullet + O_2$ ------> $ROO\bullet$ (Fast)
	(3)	$2ROO\bullet$ ------> $2RO\bullet + O_2$
	(4)	$ROO\bullet + RH$ --> $ROOH + R\bullet$ (Faster than (3))
	(5)	2ROOH —(Cat.)—> $ROO\bullet + RO\bullet + H_2O$ (Fast)
	(6)	$RO\bullet$ —> Acetone + $MeO\bullet$ (Slower than (3))

(7) $MeO\bullet + RH \rightarrow MeOH + R\bullet$

(8) $RO\bullet + RH \rightarrow ROH + R\bullet$

Termination: (9) $2RO\bullet \rightarrow ROOR$

(10) $ROOR \xrightarrow{(cat.)} \text{products (Fast) (?)}$

Comparing pure thermal with catalyzed reactions, we see that:

a) The initiation step in both cases makes water in addition to t-butyl radicals.

b) Rapid decomposition of the hydroperoxide has the effect of increasing the conversion to product by increasing the free radical flux.

c) Thus, the amount of RO• intermediate must also be greater, so the fraction of acetone should increase. In fact we make considerably more acetone in catalytic isobutane oxidation than in thermal oxidations.

d) About 10% of the RO• should go to ROOR. Since far less ROOR than this is seen, it must either be catalytically decomposed, step (10), or the catalyst must operate to prevent its formation.

Thus the catalyst for the hypothetical process shown above has at least three functions. It must initiate the reaction of isobutane, Figure 5-25. It must decompose tert-butyl hydroperoxide to TBA and O_2 (see next section). It must decompose di-tert-butyl peroxide under oxidation conditions, or otherwise prevent its formation.

5.1.10 HALOGEN SUBSTITUENT EFFECTS ON THE CATALYTIC ACTIVITY OF IRON PORPHYRIN COMPLEXES FOR THE DECOMPOSITION OF tert-BUTYL HYDROPEROXIDE

It has long been known that iron complexes are effective promoters of the decomposition of alkyl hydroperoxides (1). There has been considerable recent interest in the efficient catalytic conversion of tert-butyl hydroperoxide to tert-butyl alcohol (2-12), Eq. 1, but with currently available catalyst systems, elevated temperatures are often required and reaction selectivity is typically around 80%. Tetraphenylporphyrinatoiron(III)chloride was recently shown to be one of the more active catalysts for decomposition of tert-butylhydroperoxide (4), but in order to obtain relatively rapid rates it was necessary to either conduct reactions at somewhat elevated temperatures (60°C) or to add imidazole which resulted in a hydroperoxide decomposition catalyst that was active at room temperature.

$$ROOH \qquad ROH + 1/2\ O_2 \qquad (1)$$

In this communication we report that by halogenating the porphyrin ring of iron tetraphenylporphyrinato complexes we were able to greatly enhance catalytic activity, reduce reaction temperatures and observe reaction selectivities of 90%. Perhaloporphyrinatoiron(III) complexes gave the fastest rate of hydroperoxide decomposition by any metal complex observed to date. In fact with room temperature reaction rates of well over 100 catalyst cycles per second, these are among the fastest reactions catalyzed by a synthetic homogeneous transition metal complex in solution (14). Rates are within an order of magnitude of the activity of the catalase enzyme which decomposes hydrogen peroxide to water and oxygen (15). In addition, this study may have relevance to the mechanism of some recently disclosed rapid air-oxidations of isobutane catalyzed by iron haloporphyrin catalysts (16,17).

5.1.10.1 Procedures

Materials. Metal complexes used as catalysts: tetrakispentafluorophenylβ-octachloroporphyrinatoiron(III)chloride, $Fe(TPPF_{20}\beta\text{-}Cl_8)Cl$,tetrakispentafluoro phenylβ-octabromoporphyrinatoiron(III)chloride, $Fe(TPPF_{20}\beta\text{-}Br_8)Cl$, and tetrakispentafluorophenylporphy-rinatoiron(III)chloride, $Fe(TPPF_{20})Cl$, were prepared by methods described previously (16,17). Benzene, (99.99%), Aldrich, tert-butyl alcohol, (99.6%), Aldrich, and p-xylene, (99+%), Aldrich were used as purchased. tert-Butyl hydroperoxide (90%, 5% water, 5% tert-butyl alcohol) was used as purchased from Aldrich.

Procedures. A solution of the catalyst in p-xylene (internal standard) was quickly added to a rapidly stirring solution of tert-butyl hydroperoxide in the solvent at room temperature. Oxygen evolution was measured manometrically and liquid products were analyzed periodically by standardized gas chromatography.

5.1.10.2 Results:

Figure 5-25 compares the activity of a number of iron complexes for the decomposition of tert-butyl hydroperoxide, TBH, in benzene. It is clear that porphyrinato iron(III) complexes are quite active for catalyzing this transformation and that the extent of porphyrin ring halogenation has a dramatic effect on the catalytic activity of the porphyrinato iron(III) complex used. Very low concentrations of the perhaloporphyrin complexes $Fe(TPPF_{20}\beta\text{-}Y_8)Cl$,Y=Cl, Br were extremely effective in catalyzing room temperature TBH decomposition. Table 5-8 compares the product profile and extent of conversion of TBH in benzene after two or three hours. Selectivity to tert-butyl alcohol, TBA, was found to be 90% in all instances in which perhaloporphyrinato complexes were used as catalysts. Selectivity was lower when partially halogenated or unhalogenated porphyrins were used.

Figure 5-25 Formation of tert-butyl alcohol, TBA, from tert-butyl hydroperoxide (10 ml) in benzene (48 ml)-p-xylene (2.4 ml) using $2x10^{-4}$ mmoles of catalyst:

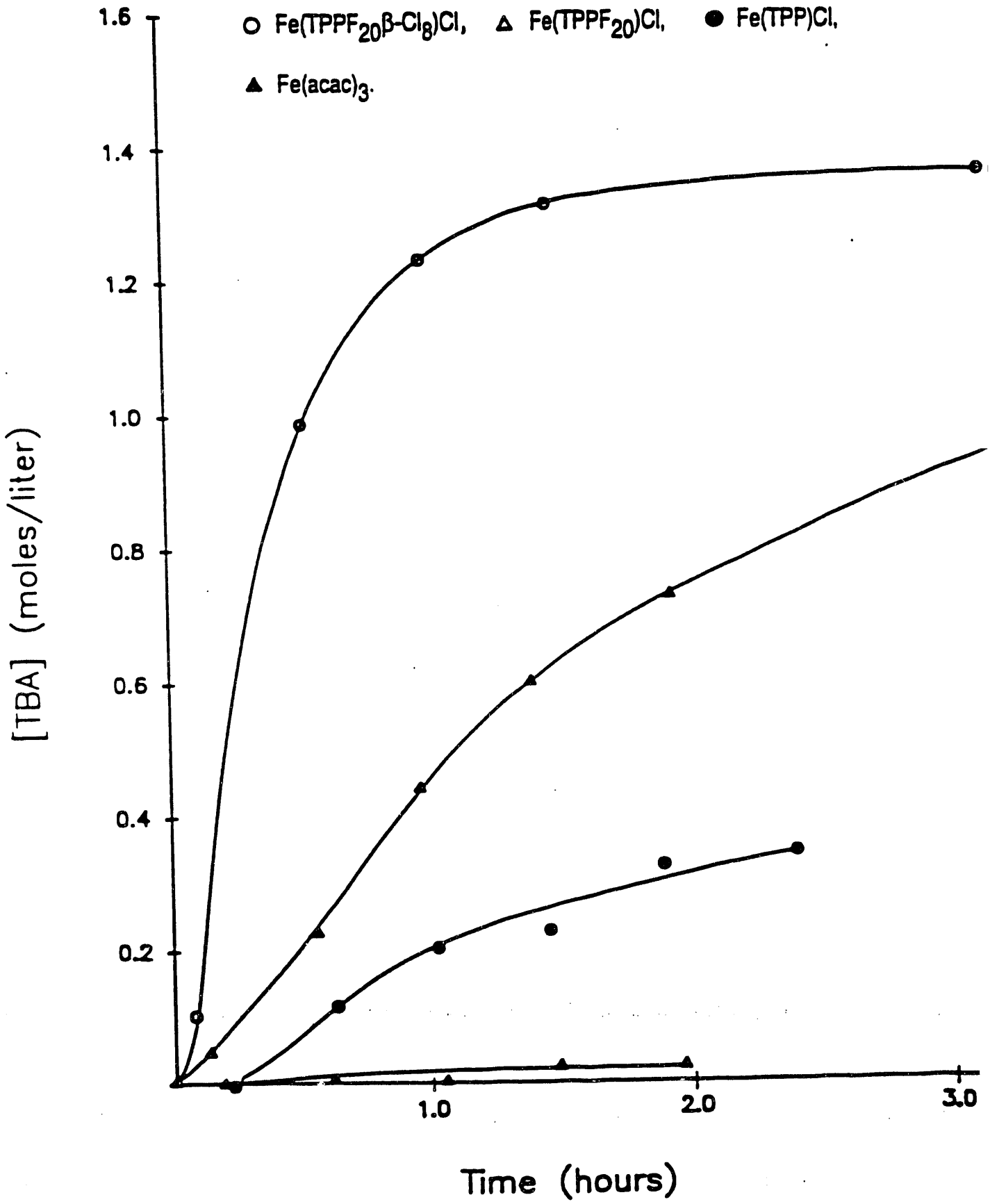

Table 5-8 Conversion of tert–Butyl hydroperoxide to tert–Butyl alcohol.

CATALYST	TIME HOURS	$tBUO_2H$ CONV.,%	– PRODUCTS, MOLAR SEL.,% – t–BuOH	$(t–BuO)_2$	$(CH_3)CO$
$Fe(acac)_3$	2.3	< 5	67	tr	32
Fe(TPP)Cl	1.9	27	82	7	11
$Fe(TPPF_{20})Cl$	3.3	72	87	10	3
$Fe(TPPF_{20}\beta\ Br_8)Cl$	1.9	95	90	8	2
$Fe(TPPF_{20}\beta\ Cl_8)Cl$	3.3	100	90	8	2

[a] The catalyst, 2×10^{-4} mmoles, in 2.4 ml p–xylene was rapidly added to a stirred solution of 10 ml $t–BuO_2$ h (90%) in 48 mls benzene. O_2 evolved was measured monometrically and liquid samples taken periodically and analyzed by standardized gc.

Kropf and Ivanov recently observed second order dependence on hydroperoxide concentration during some copper phthalocyanine complex-catalyzed decompositions of tert-butyl hydroperoxide (12) carried out at 60°C in chlorobenzene. Interestingly, these workers found that electron donation to the phthalocyanine macrocycle enhanced catalytic activity whereas electron withdrawal retarded it. Figure 5-26 shows the apparent second order dependence on hydroperoxide concentration exhibited by decompositions catalyzed by both halogenated and unhalogenated tetraphenylporphyrinatoiron(III)chloro complexes in benzene as a solvent. Incremental addition of the radical inhibitor, 2,4-di-tert-butyl-p-cresol, prolonged an induction period which grew longer by a time that was proportional to the concentration of inhibitor used, Figure 5-27. At inhibitor concentrations 10,000 fold greater than that of the iron porphyrin complex, the induction period was still less than one hour long.

5.1.10.3 Discussion

There has been much discussion in the recent literature (9,13,18) surrounding the issue of heterolytic vs. homolytic O-O bond cleavage in hydroperoxides during metalloporphyrin catalyzed hydroperoxide decomposition. It has been shown that tert-butyl hydroperoxide undergoes homolytic O-O bond cleavage in the presence of porphyrinato iron complexes (18, 19, 20). Peracidic compounds undergo heterolytic cleavage under the same conditions (18). A recent report (13) indicates that electron "push" from electron donating substituent groups on the macrocycle coupled with electron "pull" from the peroxide bound to an iron in the macrocycle result in enhanced rate of heterolytic O-O bond cleavage, Eq. 2. Electron pull from the bound peroxide is generated by electon withdrawing groups in the p-position on the aromatic peracids used in the study. These observations are reasonable since by pushing electron density from the macrocylic ligand toward the iron center one might stabilize a high-oxidation state ferryl and by removing electron density from the aromatic peracid portion of the complex one would stabilize developing negative charge.

Figure 5-26 Second order plots for the catalytic decomposition of tert-butyl hydroperoxide in benzene. ◇ $Fe(TPPF_{20}\beta\text{-}Cl_8)Cl$, △ $Fe(TPPF_{20})Cl$, ○ $Fe(TPP)Cl$.

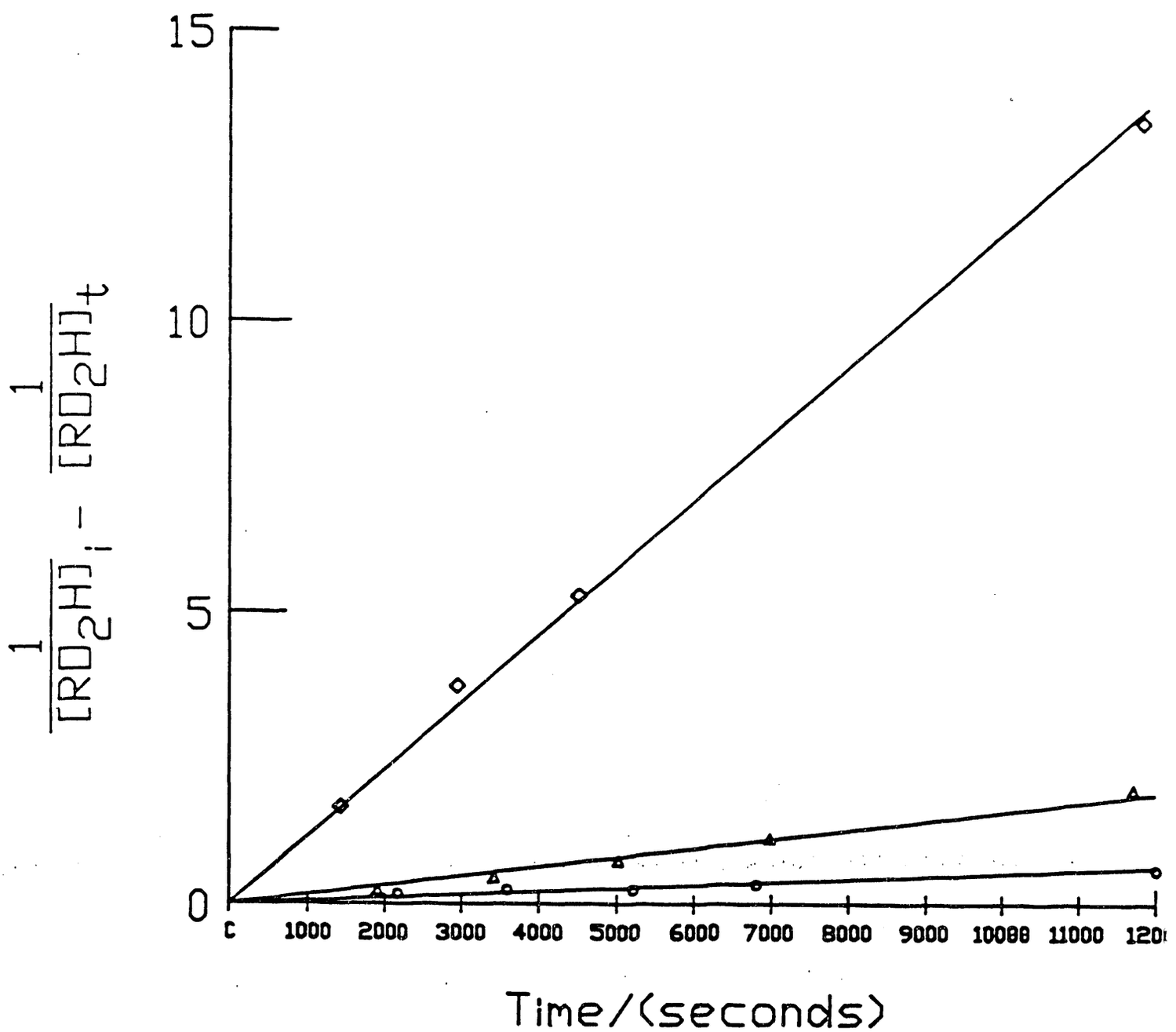

Figure 5-27 Effect of BHT on the decomposition of tert-butyl hydroperoxide (10 ml) catalyzed by $Fe(TPPF_{20}\beta\text{-}Cl_8)Cl$, $2x,10^{-4}$, mmoles, in benzene (48 ml)-p-xylene (2.4 ml).

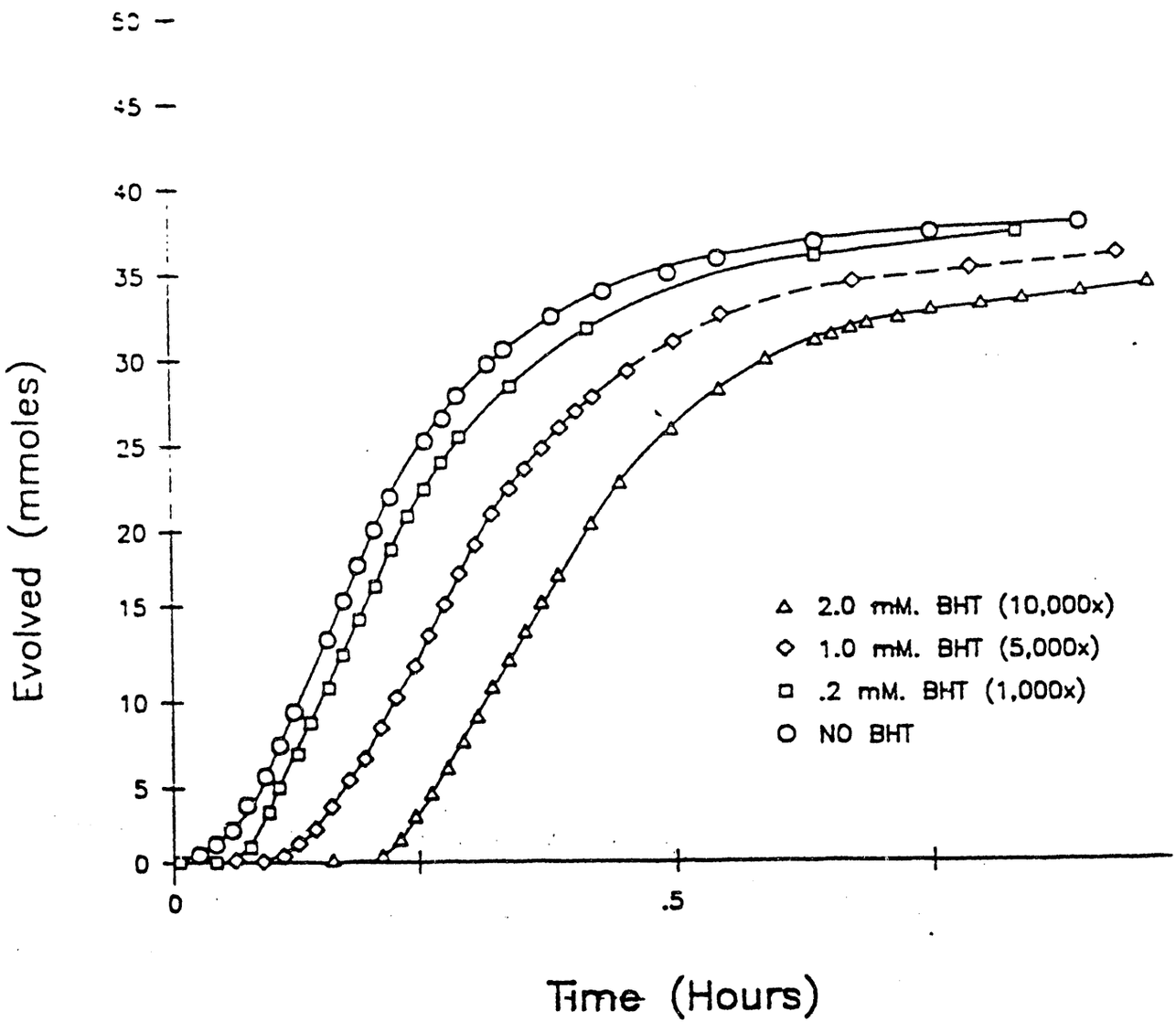

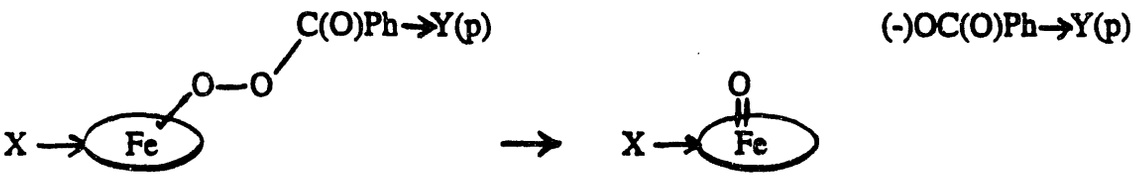

(2)

The studies reported in this communication demonstrate the effects of electron "pull" from the porphyrin macrocycle and electron "push" from the alkyl-hydroperoxide that is decomposed. Surprisingly, the result is that of greatly enhanced decomposition rates. These observations could be rationalized by a mechanism shift to homolytic O-O bond cleavage, Eq. 3, which is enhanced by electron withdrawal from the macrocyclic ligand and thus from the metal center which it surrounds. Electron withdrawal would be expected to raise the Fe(III)/Fe(II) reduction potential (16,17) and favor the homolytic O-O bond dissociation step resulting in the production of iron(II) from the iron(III) peroxy complex with release of alkylperoxy radicals. The resulting tert-butylperoxy radical could react further to produce oxygen and the tert-butoxy radical, Eq. 4, which ultimately gives TBA (9,12,18).

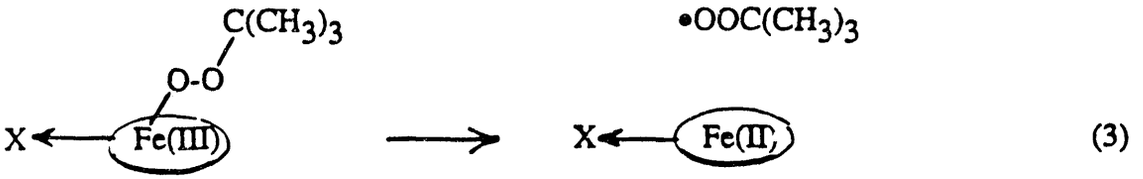

(3)

$$2\ \bullet OOC(CH_3)_3 \longrightarrow 2\ \bullet OC(CH_3)_3 + O_2 \qquad (4)$$

A catalytic reaction which is consistent with the observations presented above can be envisioned as proceeding via the pathway shown in Scheme 5-28, below. Early studies of metal complex catalyzed hydroperoxide decomposition were rationalized based on M(III)/M(II) catalysis via the well known Haber-Weiss cycle shown in Figure 5-28.

More recent studies, however, have indicated that metal oxo species may be involved (18-21) in metalloporphyrin-catalyzed alkylhydroperoxide decomposition.

FIGURE 5-28

HABER WEISS DECOMPOSITION OF HYDROPEROXIDES USING METALLOPORPHYRINS AS CATALYSTS (PORPHYRIN RING OMITTED)

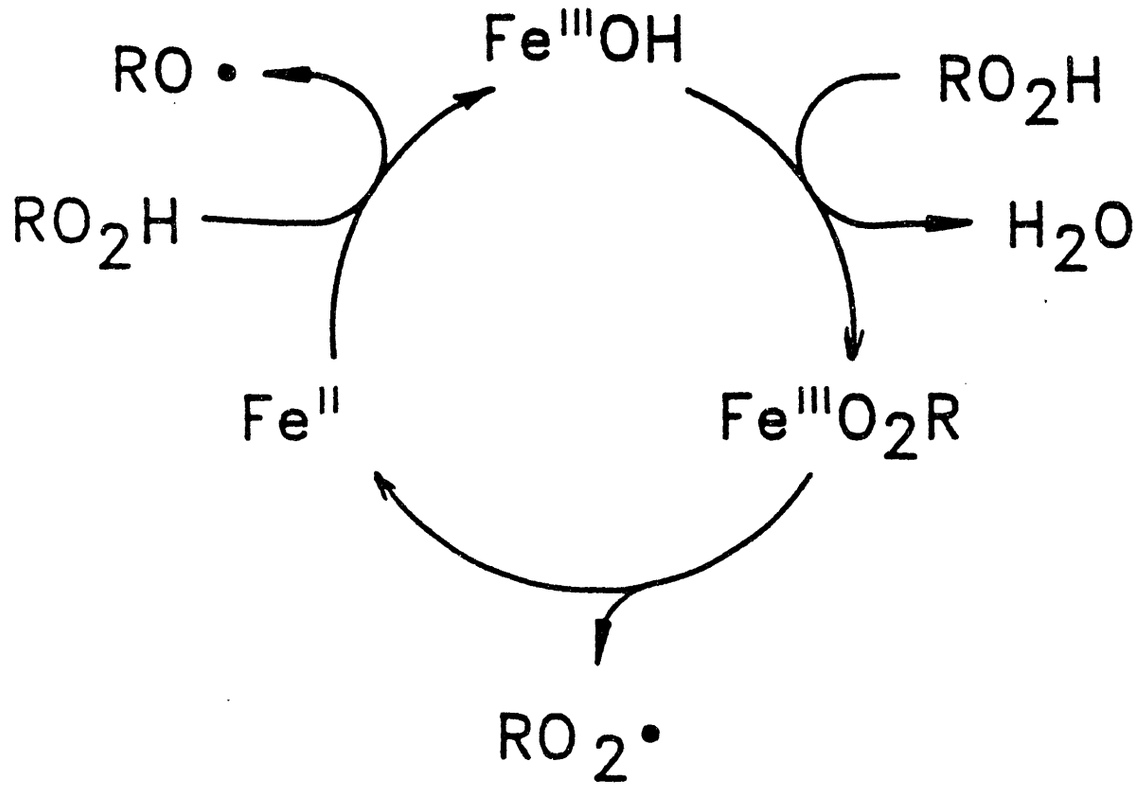

$$2RO_2H \longrightarrow RO_2\bullet + H_2O$$

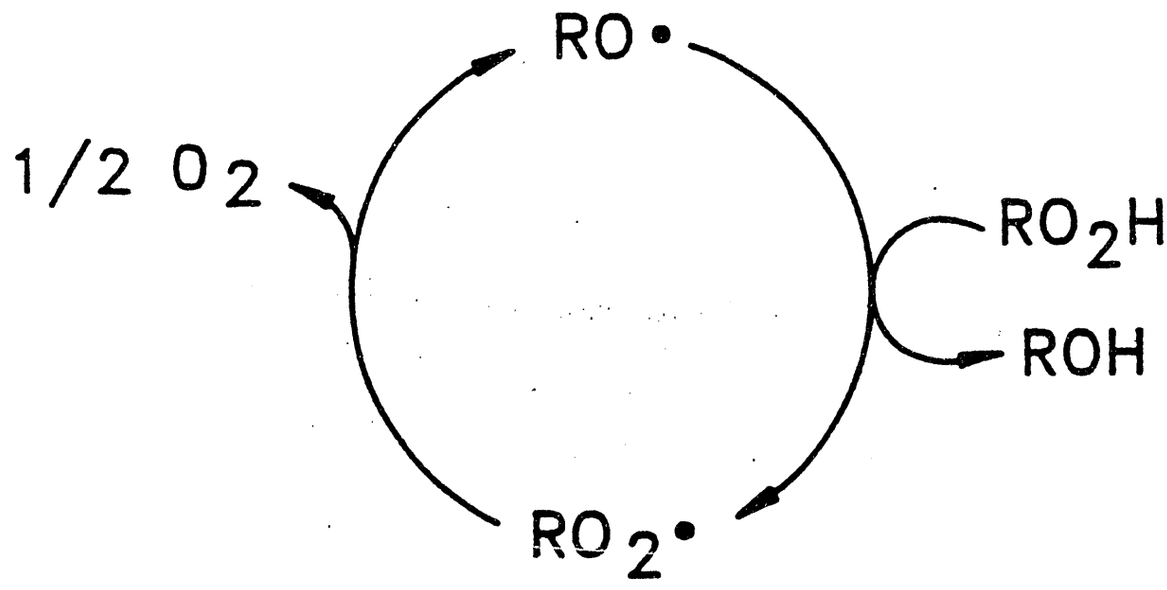

Balch and his co-workers have found (19) that Fe(TPP)OH reacts stoichiometrically with tert-butylhydroperoxide to form the alkylperoxy iron(III) complex suggested in Figure 5-28. In the presence of a suitable base (19) this complex homolyzes to form not Fe(II), but the ferryl complex, Eq.5. Figure 5-29 shows the possible generation of alkoxy and alkylperoxy radicals by a mechanism in which no iron(II) species take part, but rather the catalysis occurs via a one-electron homolytic Fe(III)/Fe(IV)=O couple. At this time it is not possible to assess the relative contributions from pathways shown in Figures 5-28 and 5-30.

$$(TPP)FeOO(t\text{-}Bu) + B \qquad (B)(TPP)Fe(IV)=O + t\text{-}BuO\bullet \qquad (5)$$

The similarity between the effects of reduction potential on catalytic activity for both the decomposition of tert-butyl hydroperoxide to tert-butyl alcohol and the air-oxidation of isobutane (16, 17) to tert-butyl alcohol raises the possibility that these reactions have pathways in common. We continue to pursue the synthetic potential of this reaction, extend the trends in catalytic activity with increasing reduction potential, and consider possible implications of this work for air oxidations using perhaloporphyrin catalysts.

FIGURE 5-29

POSSIBLE METAL OXO PATHWAYS FOR DECOMPOSITION OF HYDROPEROXIDES
USING METALLOPORPHYRIN CATALYSTS (PORPHYRIN RING OMITTED)

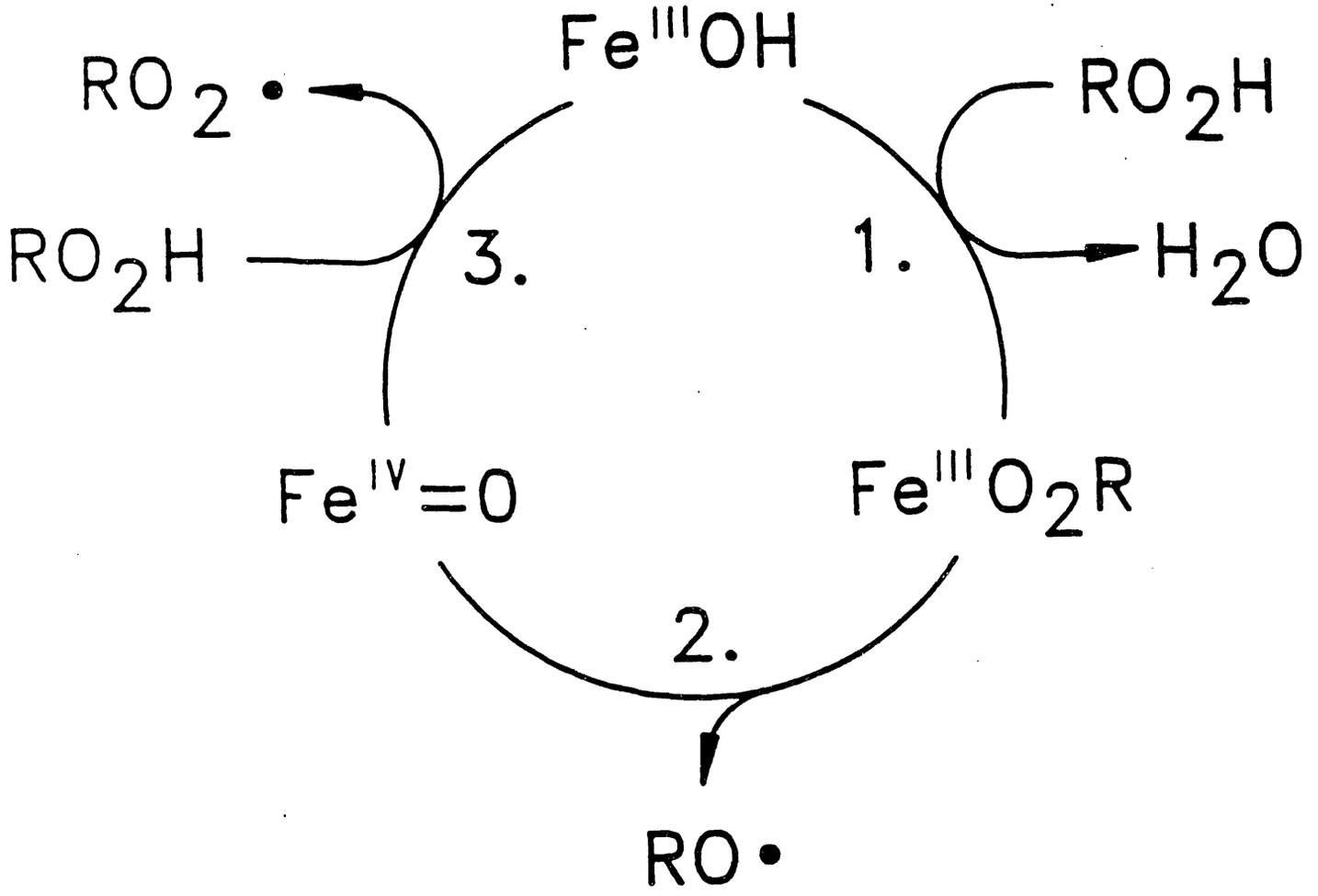

5.1.10.4 REFERENCES

1. Sosnovsky, G. and Rawlinson, D.J.,"Organic Peroxides", D. Swern, Ed. Wiley, New York, pp 153-268, 1971.

2. J.R. Sanderson, E.T. Marquis, U.S. Patent 4,922,035, May 1, 1990.

3. Sanderson, J.R., Marquis, E.T. and Knifton, J.F., U.S. Patent 4,922,036, May 1, 1990.

4. Sanderson, J.R., Marquis, E.T. and Mueller, M.A., U.S. Patent 4,922,034, May 1, 1990.

5. Sanderson, J.R., Knifton, J.F. and Marquis, E.T., U.S. Patent 4,922,033, May 1, 1990.

6. Sanderson, J.R., Knifton, J.F., Marquis, E.T. and Mueller, M.A., U.S. Patent 4,912,256, Mar. 27, 1990.

7. Sanderson, J.R. and Knifton, J.F., U.S. Patent 4,910,349, Mar. 20, 1990.

8. Sanderson, J.R., U.S. Patent 4,712,267, Mar. 27, 1990.

9. Bruice, T.C., Acc. Chem. Res., 24, 243 (1991).

10. Barton, D.H.R., Beviere, S.D., Chavasiri, W., Csuhai, E., Doller, and Liu, W.G., J. Amer. Chem. Soc., 114. 2147 (1992).

11. Sawada, H., Shigaki, H. Kato, M and Nakayama, M., Bull. Chem. Soc. Jpn., 64, 785 (1991).

12. Kropf., H. and Ivanov, S.K., Oxidation Commun., 13, 23 (1990).

13. Yamaguchi, K., Watanabe, Y., and Morishima, I., Inorg. Chem., 31, 157 (1992).

14. Parshall, G.W., "Homogeneous Catalysis", Wiley, N.Y., p.177, 1980.

15. Hoffmann, P. and Meunier, R.B., Bull. Soc. Chim. Fr., 129, 85 (1992).

16. Lyons, J.E. and Ellis, P.E., Jr., Catalysis Letters, 8, 45 (1991).

17. Ellis, P.E., Jr. and Lyons, J.E., Coord. Chem. Rev., 105, 181 (1990).

18. Lee, W.E. and Bruice, T.C., J. Amer. Chem. Soc., 107, 513 (1985).

19. Balch, A.L., Hart, R.L., Latos-Grazynski, L, and Traylor, T.G., J. Amer. Chem. Soc., 112, 7382 (1990).

20. Traylor, T.G. and Xu, F., J. Amer. Chem. Soc., 109, 6201 (1987).

5.3 METALS IN REGULAR OXIDIC MATRICES

5.3.1 DEVELOPMENT AND APPLICATION OF A KINETIC MODEL FOR OXIDATION OF METHANE.

5.3.1.1 Summary and Conclusions

This section condenses initial work on modeling the homogeneous oxidation of methane, covering the basic 1-carbon set of reactions and expansion to include 2-carbon kinetics in both plug-flow (or batch) and back-mixed reactors. As a general example, we use the reaction of 3:1 methane:air at 400°C and 815 psi, which approximates many of the laboratory experiments. For applying the models, our target was to find a process which converts at least 20% of the methane to methanol at 80% selectivity.

The basic model is a set of 61 equations, updated from work of Bedeneev, et. al., solved for given conditions by SIMUSOLV, a commercial batch (or plug-flow) isothermal process simulator. Calculating all 19 species, the model finds that the oxidation starts slowly and builds up to a high rate which drops off quickly as the oxygen is depleted. Detailed examination of all reactions confirms that the main path is oxygen combining with methyl radicals to ultimately make methoxy radical, which abstracts hydrogen from methane to form methanol and make new methyl radical. Branching comes from splitting peroxy compounds into two radicals. Most of the competing oxidation to carbon monoxide and water proceeds by abstracting hydrogen from methanolic carbon. Over the range 380-450°C, methanol selectivity is favored by high temperature, low oxygen, and high methane. The model was adjusted to lower the oxidation rate by solid glass surface; however, it seems to overcorrect for high surface solids.

One accepted path for catalysis of methane oxidation is formation and emission of methyl radicals, the simulation of which is possible by adding that reaction to the model. Adjusting the rate constant to higher and higher values showed methanol selectivity going through a maximum and followed first by formaldehyde and finally by ethane. Nearly 80% methanol at 4% methane conversion is made at 2.5% oxygen, but selectivity drops at higher oxygen (and conversion). Thus, our commercial target is not likely to be obtained solely with this type of catalysis in a plug-flow reactor. The model gives good agreement with the few sets of homogeneous conditions reported in the literature. The exception is the 1988 paper by Gesser and coworkers; however, they subsequently reported reactor instability.

5.3.1.2 Basic Model for Methane Oxidation

This model, the workhorse of our program, has been used to examine the overall course of the homogeneous oxidation, rank the importance of reactions, look at the effect of variables, check the impact of adding solid surfaces, predict the results of catalysis, and interpret experimental results.

5.3.1.2.1 The Model Basics

The original set of reactions for this model was taken from a paper by Bedeneev, Gol'denberg, Gorban, and Teitel'boim, Kin & Kat (Trans) 29 7-13 (1988). In the present set, displayed in Table 5-9, only Reactions 14 and 53 have been updated; however, the new rate constant for #14, $CH_3O\bullet + CH_4 = CH_3OH + CH_3\bullet$, increases the selectivity to methanol from 30 to 58% when charging 25% air in methane at 400°C and 850 psi. The new rate constant for #53 is about 3 times larger than the old but has less effect on the overall production of carbon dioxide.

TABLE 5-9

RATE CONSTANTS FOR GAS PHASE METHANE OXIDATIONS

	Con	A	E	380 C	390 C	400 C
1. $CH_4 + O_2 = CH_3 + HO_2$	K1	1E-10	-55972	1.862103E-29	3.568119E-29	6.706309E-29
2. $CH_3 + HO_2 = CH_4 + O_2$	K2	1E-12	0.00	1E-12	1E-12	1E-12
3. $CH_3 + O_2 = CH_3OO$	K3	2E-12	0.00	2E-12	2E-12	2E-12
4. $CH_3OO = CH_3 + O_2$	K4	8.9E+13	-31285	3023.030137	4348.175427	6187.018059
5. $OH + CH_4 = H_2O + CH_3$	K5*	1.32E-17	-2688	4.226E-13	4.489E-13	4.7821E-13
6. $CH_3OO = 2CH_3O + 0_2$	K6	1.71E-13	0.00	1.71E-13	1.71E-13	1.71E-13
7. $2CH_3OO = CH_2O + CH_3OH + O_2$	K7	7.4E-14	0.00	7.4E-14	7.4E-14	7.4E-14
8. $CH_3OO + CH_3 = 2CH_3O$	K8	4.5E-11	0.00	4.5E-11	4.5E-11	4.5E-11
9. $CH_3OO + HO_2 = CH_3OOH + O_2$	K9	7.7E-14	2599	5.704244E-13	5.534565E-13	5.374753E-13
10. $CH_3 + HO_2 = CH_3O + OH$	K10	3E-11	0.00	3E-11	3E-11	3E-11
11. $2HO_2 = H_2O_2 + O_2$	K11	2.2E-13	1230	5.6757E-13	5.595165E-13	5.518114E-13
12. $2CH_3 = C_2H_6$	K12	4E-11	0.00	4E-11	4E-11	4E-11
13. $CH_3O + HO_2 = CH_3OH + O_2$	K13	1.7E-11	0.00	1.7E-11	1.7E-11	1.7E-11
14. $CH_3O + CH_4 = CH_3OH + CH_3$	K14**	1.7E-10	-14863	1.8068E-15	2.1473E-15	2.5309E-15
15. $CH_3O + O_2 = CH_2O + HO_2$	K15	1E-13	-2599	1.349872E-14	1.391257E-14	1.432624E-14
16. $CH_3O = CH_2O + H$	K16	1E+14	-29986	9241.422637	13093.285546	18359.588310
17. $CH_3OO + CH_4 = CH_3OOH + CH_3$	K17	1E-12	-21491	6.433299E-20	8.258052E-20	1.052203E-19
18. $CH_3OO + CH_2O = CH_3OOH + CHO$	K18	4.7E-13	-11995	4.551899E-17	5.232624E-17	5.990295E-17

TABLE 5-9 (Con't)

RATE CONSTANTS FOR GAS PHASE METHANE OXIDATIONS

19.	$HO_2 + CH_2O = H_2O_2 + CHO$	K19	2E-12	-10994	4.188812E-16	4.75956E-16	5.387589E-16
20.	$CH_3 + CH_2O = CH_4 + CHO$	K20	1.4E-12	-6952	6.603431E-15	7.158953E-15	7.74266E-15
21.	$CH_3O + CH_2O = CH_3OH + CHO$	K21	1E-12	-3598	6.251666E-14	6.518555E-14	6.7884E-14
22.	$OH + CH_2O = H_2O + CHO$	K22	1.25E-11	-174	1.093161E-11	1.095373E-11	1.097524E-11
23.	$H + CH_4 = H_2 + CH_3$	K23	1.3E-10	-11921	.33291E-14	1.530927E-14	1.751139E-14
24.	$H + O_2 + M = HO_2 + M$	K24	1E-32	909	2.014559E-32	1.993394E-32	1.973071E-32
25.	$H + CH_2O = H_2 + CHO$	K25	3.27E-11	-3667	1.938447E-12	2.022822E-12	2.108199E-12
26.	$CHO + O_2 = CO + HO_2$	K26*	5.5E-11	0.00	4.1149E-12	4.0899E-12	4.0655E-12
27.	$CHO + M = CO + H + M$	K27	4E-10	-16992	8.2414E-16	1.004021E-15	1.21601E-15
28.	$CH_3OOH = CH_3O + OH$	K28	4E+15	-42979	16.593244	27.340345	44.384696
29.	$H_2O_2 = 2OH$	K29	3E+14	-48958	0.012423	0.021942	0.038105
30.	$OH + H_2 = H_2O + H$	K30*	1.06E-17	-1488	1.4369E-12	1.5070E-12	1.5791E-12
31.	$HO_2 + H_2 = H_2O_2 + H$	K31	5.6E-12	-22289	1.947986E-19	2.523809E-19	3.244782E-19
32.	$CH_3OO + H_2 = CH_3OOH + H$	K32	3.6E-12	-22289	1.252277E-19	1.622448E-19	2.085931E-19
33.	$CH_3O + H_2 = CH_3OH + H$	K33	3.6E-12	-9986	1.639351E-15	1.841033E-15	2.060411E-15
34.	$CH_3 + H_2 = CH_4 + H$	K34	3.6E-12	-10789	8.830044E-16	1.000931E-15	1.13039E-15
35.	$CH_3OO + CH_3O = CH_3OOH + CH_2O$	K35	1.5E-12	0.00	1.5E-12	1.5E-12	1.5E-12
36.	$CH_4 + HO_2 = CH_3 + H_2O_2$	K36	3E-12	-21491	1.92999E-19	2.477416E-19	3.156609E-19
37.	$CH_3 + CH_3OH = CH_4 + CH_2OH$	K37	3.3E-13	-9795	1.740997E-16	1.95085E-16	2.178618E-16
38.	$CH_3OO + CH_3OH = CH_3OOH + CH_2OH$	K38	5E-13	-14393	7.631648E-18	9.020812E-18	1.060999E-17

TABLE 5-9 (Con't)

RATE CONSTANTS FOR GAS PHASE METHANE OXIDATIONS

39.	$CH_2OH + O_2 = CH_2O + HO_2$	K39	2E-12	0.00	2E-12	2E-12	2E-12
40.	$HO_2 + CH_3OH = H_2O_2 + CH_2OH$	K40	1.5E-12	-14393	2.289494E-17	2.706244E-17	3.182998E-17
41.	$OH + CH_3OH = H_2O + CH_2OH$	K41	5.7E-12	-1400	1.938175E-12	1.96995E-12	2.001288E-12
42.	$OH + CH_3OH = H_2O + CH_3O$	K42	1.7E-11	-3299	1.338134E-12	1.390421E-12	1.443107E-12
43.	$CH_3O + CH_3OH = CH_3OH + CH_2OH$	K43	6.6E-13	-5296	1.115155E-14	1.18593E-14	1.258893E-14
44.	$H + CH_3OH = H_2 + CH_2OH$	K44	2.16E-11	-5256	3.763834E-13	4.00085E-13	4.245083E-13
45.	$H + H_2O_2 = OH + H_2O$	K45	3E-10	-6297	2.34394E-12	2.521862E-12	2.707397E-12
46.	$OH + H_2O_2 = H_2O + HO_2$	K46	3.7E-12	-516	2.486176E-12	2.501126E-12	2.515718E-12
47.	$H + H_2O_2 = H_2 + HO_2$	K47	1.7E-11	-4998	3.61377E-13	3.829839E-13	4.05183E-13
48.	$CH_3OO + H_2O_2 = CH_3OOH + HO_2$	K48	2.5E-13	-12993	1.122206E-17	1.305075E-17	1.510951E-17
49.	$CH_3O + H_2O_2 = CH_3OH + HO_2$	K49	2.5E-13	-3990	1.155474E-14	1.210302E-14	1.265987E-14
50.	$CH_3 + H_2O_2 = CH_4 + HO_2$	K50	2.5E-13	-2797	2.897181E-14	2.99288E-14	3.088757E-14
51.	$OH + CO = H + CO_2$	K51*	2.5E-17	764	2.0565E-13	2.0790E-13	2.1016E-13
52.	$HO_2 + CO = OH + CO_2$	K52	1.7E-10	-22981	3.469618E-18	4.531522E-18	5.871665E-18
53.	$CH_3O + CO = CH_3 + CO_2$	K53**	1.83E-12	-6939	8.718522E-15	9.450552E-15	1.021954E-14
54.	$2CH_3O = CH_3OH + CH_2O$	K54	3E-11	0.0	3.8E-11	3.8E-11	3.8E-11
55.	$CH_3 + CH_3O = CH_4 + CH_2O$	K55	2.8E-11	0.00	2.8E-11	2.8E-11	2.8E-11
56.	$CH_3 + Solid = (1.5H_2 + xCO + yCO_2)$	K56	0.005z	0.00			
57.	$CH_3OO + Solid = (1.5H_2O + xCO + yCO_2)$	K57	0.005z	0.00			
58.	$HO_2 + Solid = (.5H_2O + O_2)$	K58	0.005z	0.00			

TABLE 5-9 (Con't)

RATE CONSTANTS FOR GAS PHASE METHANE OXIDATIONS

59.	CH_3OOH + Solid=($1.5H_2O$+xCO+yCO_2)	K59	0.005z	0.00
60.	H_2O_2 + Solid = (H_2O+.5O_2)	K60	0.0015z	0.00
61.	H_2O_2 + Solid = (H_2O+.5O_2)	K61	0.0015z	0.00

where z = (3.23E11 exp(-31600/RT))(1.574/DIA+[SA]1.4E4) for DIA = diameter of quartz reactor in inches, SA = surface area of quartz packing in sq. meters/cc.

(1) Bedeneev et al, Transl. from Kin & Kat 29 7-13 (1988).

* Factor T^x in rate constant where for K5, x = 1.92; K26, x = -0.4; K30, x = 2; K51, x = 1.3.

** K14 from Los Alamos: Wantuck et al, 22nd Int. Symp. on Comb. Seattle, 8/14/88. TIC Abst. 1582580 of TIC Report LA-UR-88-186. K53 calculated from Wantuck, et al, Chem Phys Let 138 548-52 (1987).

NOTE: IN THIS TABLE E MEANS THE EXPONENTS OF 10; THUS, E-14 = 10^{-14}. EXP IS USED TO DESIGNATE THE NATURAL BASE; THUS, EXP-14 MEANS NATURAL BASE e^{-14}.

Simusolv, a commercial modelling and simulation software, was used to solve the 61 differential equations by Gear stiff integration. We have found that running the integration for a very short time, less than 1% of the total run time, serves to initialize all of the species and allow trouble-free operation for the rest of the run. Also, adding an adjustable factor common to all of the rate constants allows the time scale to be shifted to smaller units, thereby enabling operation at extremes of variables including run time and temperature.

5.3.1.2.2 Air Oxidation of Methane

The simple model is batch, starting from zero time with a premixed, preheated gas at constant temperature and pressure. (Because expansion or contraction of volume is always less than 2%, the same data can be used for a plug-flow reactor at various residence times.) Typically, the test reaction in this report will be 3:1 methane:air at 400°C and 815 psi. Figures 5-30, 5-31, and 5-32 illustrate the course of the oxidation according to the model:

1. The oxygen curve in Figure 5-30 shows that oxidation is quite slow at first and increases rapidly as the radicals build up, so that only 15 % of the oxygen is used up in the first 8 seconds and then completely exhausted in the next 8 seconds. This means that, in the final stages, the experimenter cannot easily stop the reaction reproducibily short of completion. Most of the published data are taken at very long residence times, presumably where the results can be repeated. Only recently has there been a report (Ritz and Baiker, I.E.C. Res. 30 2287 [1991]) where space velocities have been sufficiently high to examine the early stages of the reaction. Unfortunately, the preheated gases were not premixed, so that their initially high ethylene yield cannot be compared to our model.

2. An interesting feature of the model reaction is the long "tail" which keeps on going long after the oxygen has been exhausted. The reason for this behavior is hydrogen peroxide which builds up and and then decays to produce radicals. Experimentally, little or no peroxide is observed, perhaps because of:

FIGURE 5-30

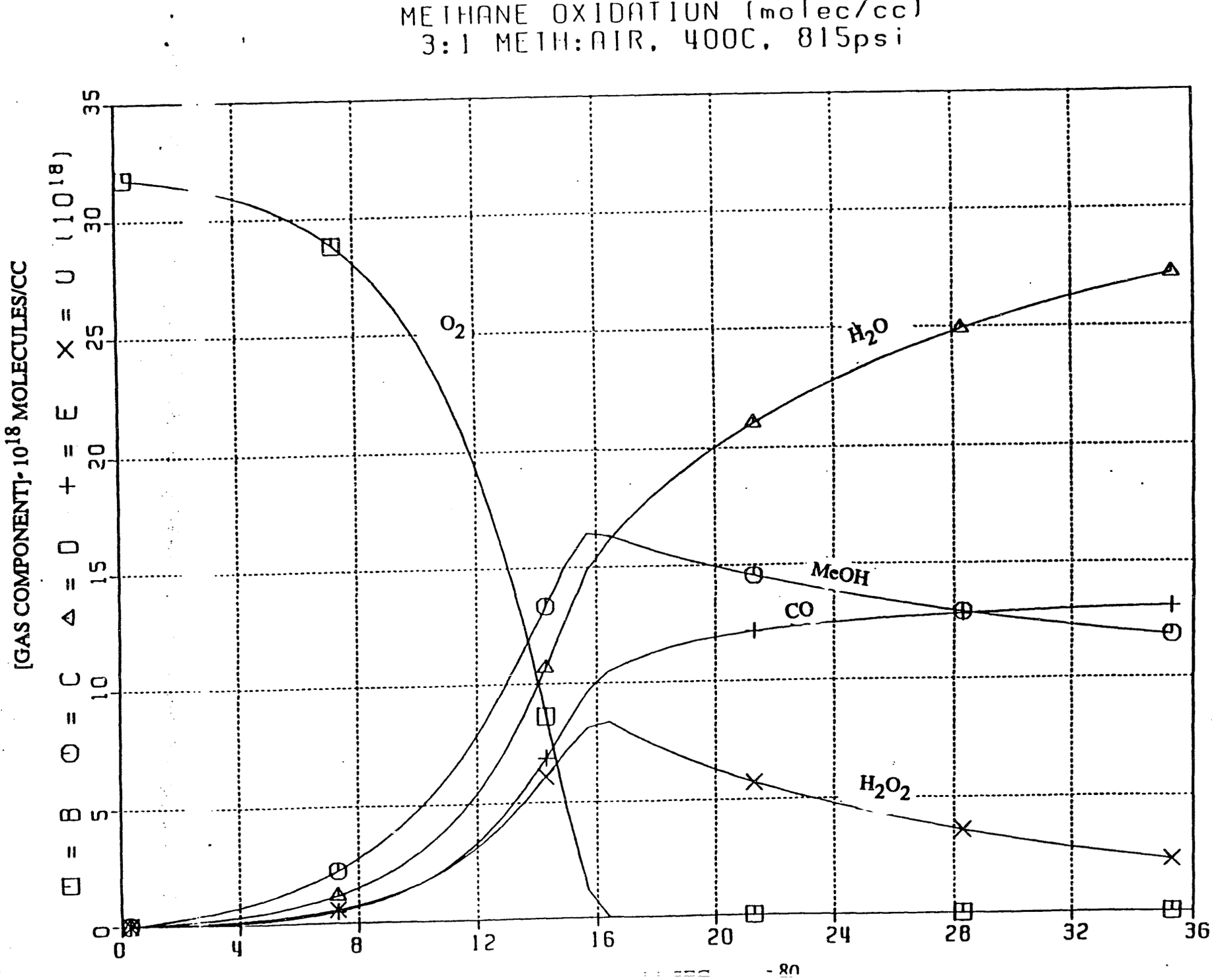
METHANE OXIDATION (molec/cc)
3:1 METH:AIR, 400C, 815psi
[GAS COMPONENT]• 10^18 MOLECULES/CC
□ = B ○ = C △ = D + = E × = U (10^18)
O2
H2O
MeOH
CO
H2O2
0
4
8
12
16
20
24
28
32
36
0
5
10
15
20
25
30
35

a. Very long residence times so that the peroxide decomposes before the reaction is quenched.

b. Error in some of our rate constants.

c. Catalyzed decomposition of the peroxide by surfaces either in or after the reactor. Many solids are known to be active.

3. Figures 5-30 and 5-31 illustrate what happens to all species in the reaction. When the oxygen is being consumed, the products increase while intermediates generally rise and then decline. After oxygen is gone (about 16.5 sec), the reaction changes dramatically. Peroxides decline, methanol and formaldehyde are consumed, and the important products become ethylene, hydrogen, and $\bullet CH_2OH$. During regular oxidation, concentrations of H and OH are very low; $\bullet CH_3$, $\bullet CHO$ and $\bullet CH_2OH$ low; $HO_2\bullet$ is higher; and $CH_3O\bullet$ is very high. Upon depletion of the oxygen, $\bullet CH_2OH$ becomes the most stable intermediate.

4. Variation of the product distribution with time appears in Figure 5-32, along with the methane conversion, which with 3:1 methane:air grows to about 6.7%. Note that the post-oxygen reaction drops methanol selectivity from an encouraging 55% to 44%, so that the existence of a 'tail' becomes an important consideration. Experimentally, one generally sees lower methanol, low hydrogen peroxide, low formaldehyde and high carbon dioxide; so, perhaps the 'tail' is taking place at the very long residence times customarily employed. It is interesting that formaldehyde starts out as 30% of the product and drops continuously to 1% or less.

FIGURE 5-31

METHANE OXIDATION - FORMATION OF INTERMEDIATES WITH TIME

(a)

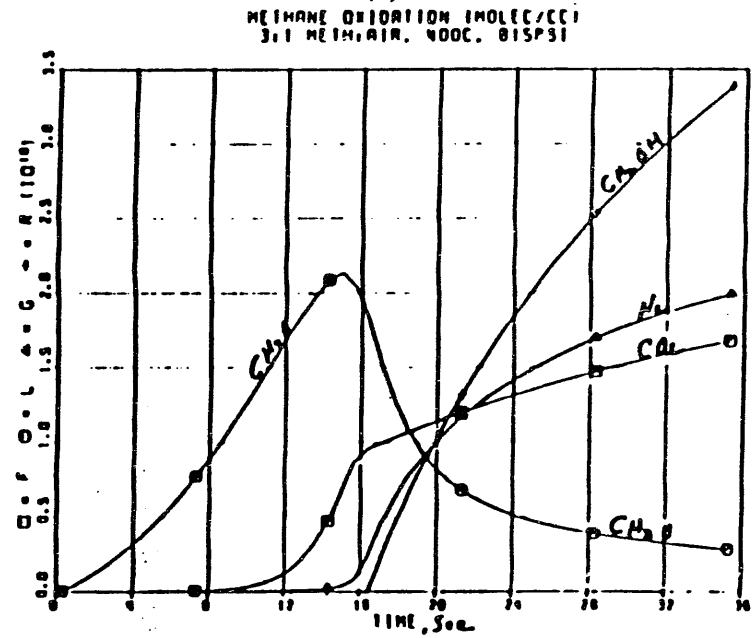

(b)

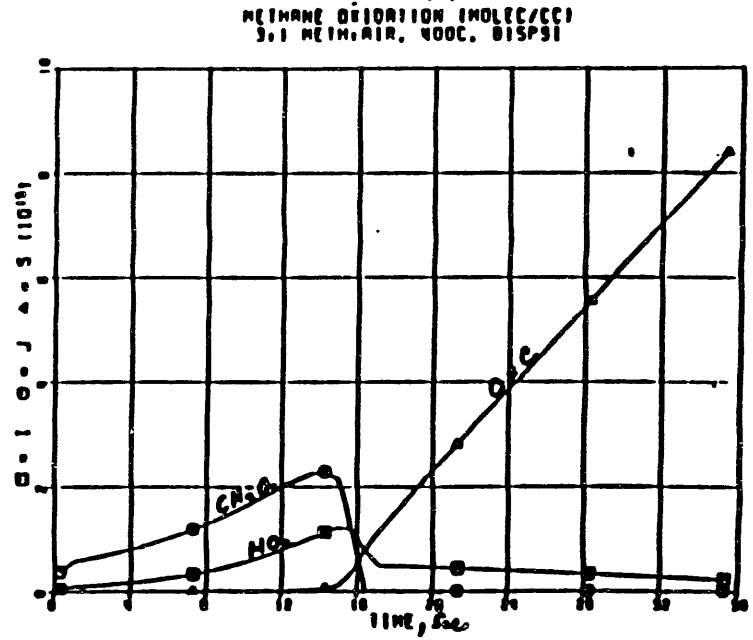

(c)

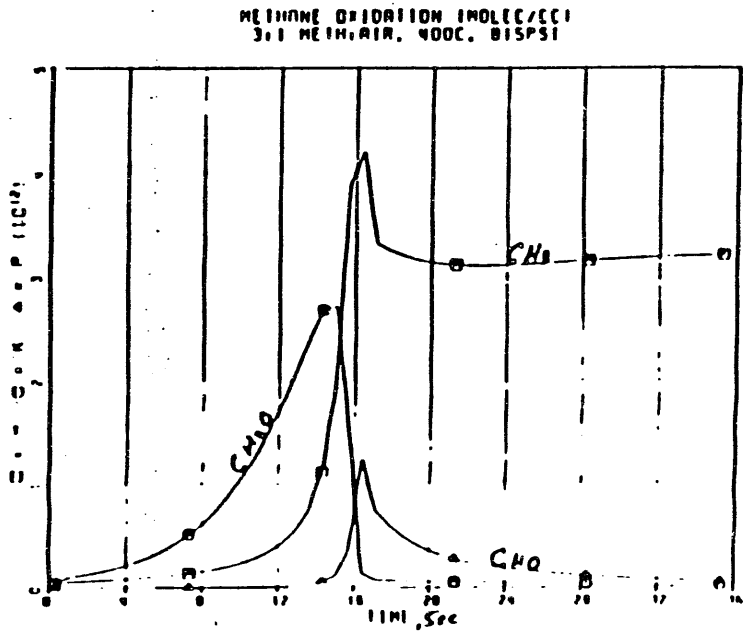

(d)

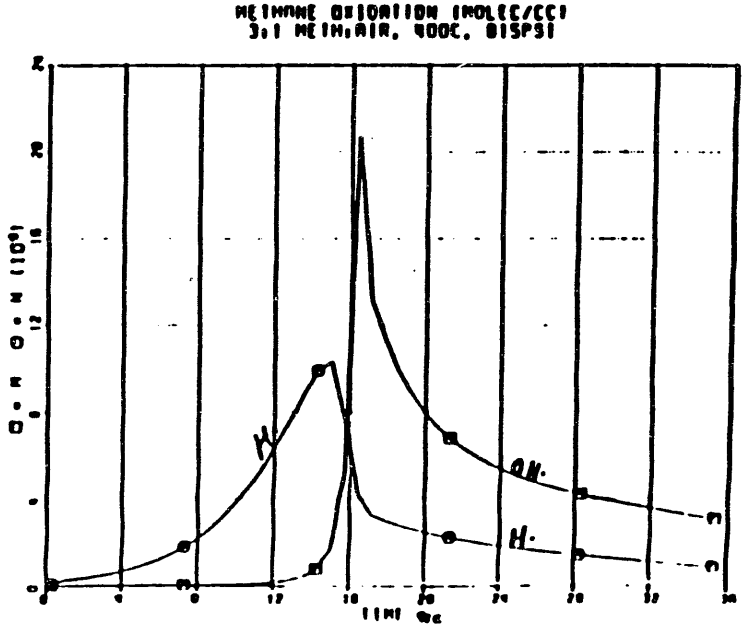

FIGURE 5-32

METHANE OXIDATION - % CARBON SELECTIVITY OF PRODUCTS

3:1 METH:AIR, 400C, 815PSI

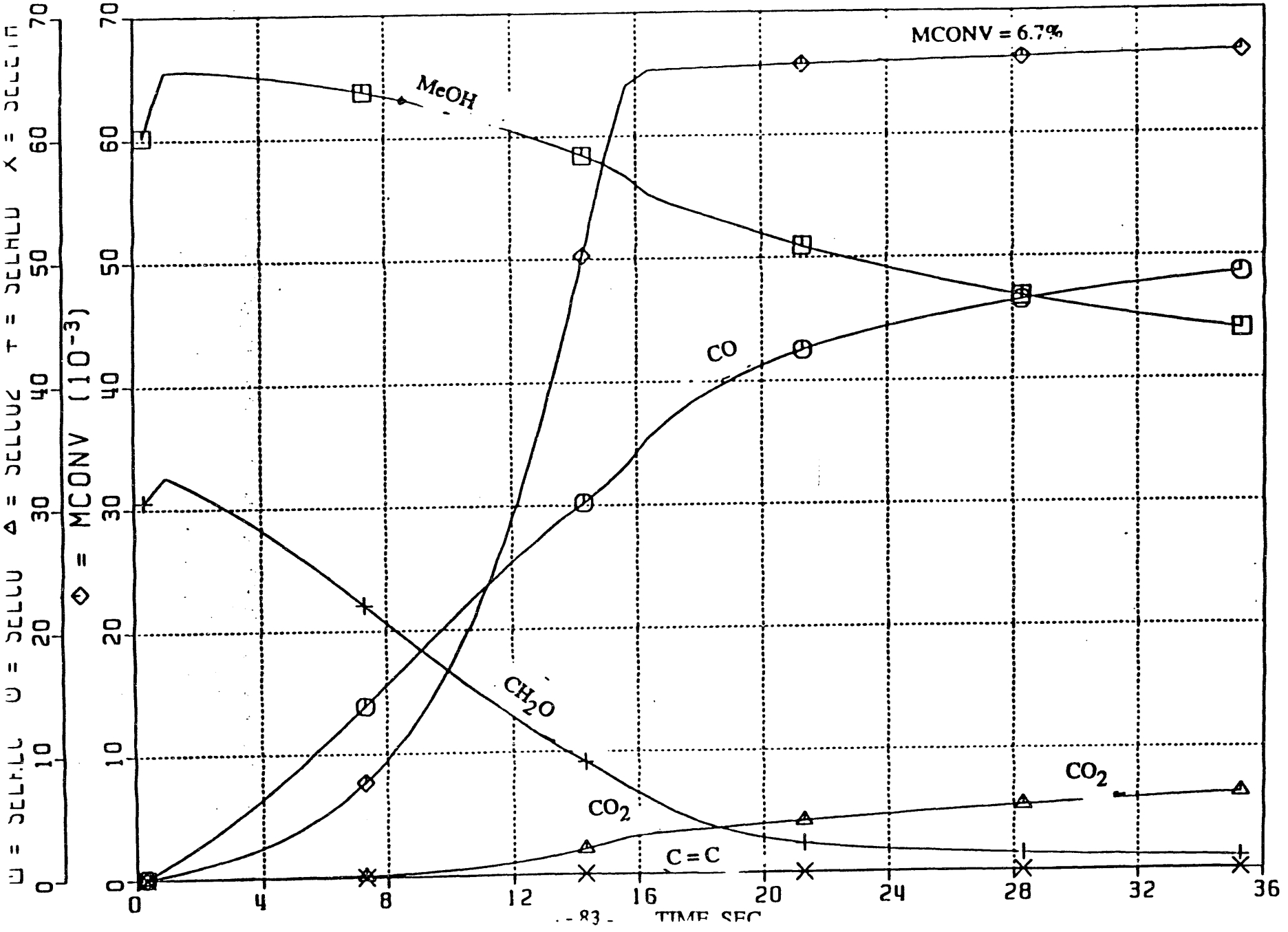

5.3.1.2.3 Important Reactions In The Oxidation

The step-wise single-electron oxidation of methane to methanol requires Removal of one hydrogen to $\bullet CH_3$, conversion somehow to $CH_3O\bullet$, followed by abstraction of H to produce methanol. Working backwards, we looked at the important sources of $CH_3O\bullet$ which are $CH_3OO\bullet$ and CH_3OOH. These, in turn, are made from $\bullet CH_3$ by addition of oxygen molecule. To get a precise picture, we asked Simusolv to calculate the % contribution of all the reactions which make or destroy CH_3OH, $CH_3O\bullet$, $CH_3OO\bullet$, CH_3OOH, and $\bullet CH_3$. The simplified Table 5-10 lists the predominant reactions.

As expected, the model pictures the familiar autoxidation model for oxidation of methane to methanol:

Initiation: $CH_4 + O_2 = CH_3 + HO_2$

Propagation: $CH_3 + O_2 = CH_3OO$

$2\ CH_3OO = 2\ CH_3O + O_2$

$CH_3OO + CH_4 = CH_3OOH + CH_3$

$CH_3OOH = CH_3O + OH$ (Chain-Branching)

$CH_3O + CH_4 = CH_3OH + CH_3$

Side reactions are the abstraction of hydrogen from both $CH_3O\bullet$ and methanol to yield fomaldehyde and $\bullet CH_2OH$, followed by further oxidation to carbon oxides and water. Modest changes in temperature and/or pressure can have significant effect on the competitive reactions.

TABLE 5-10

RELATIVE IMPORTANCE OF REACTIONS, PER CENT
3:1 Methane:Air

Reaction	815# 380C	815# 400C	815# 420C	1015# 400C
Make Methanol				
14. $CH_3O + CH_4 = CH_3OH + CH_3$	66	81	63	72
7. $2CH_3OO = CH_2O + CH_3OH + O_2$	8	14	7	11
43. $CH_3O + CH_3OH = CH_3OH + CH_2OH$	12	2	13	6.1
Destroy Methanol				
40. $HO_2 + CH_3OH = H_2O_2 + CH_2OH$	29	28	25	28
43. $CH_3O + CH_3OH = CH_3OH + CH_2OH$	27	18	29	24
38. $CH_3OO + CH_3OH = CH_3OOH + CH_2OH$	17	38	14	24
41. $OH + CH_3OH = H_2O + CH_2OH$	16	10	22	14
Make Methoxy				
28. $CH_3OOH = CH_3O + OH$	51	28	67	48
6. $2CH_3OO = 2CH_3O + O_2$	34	44	26	47
Destroy Methoxy				
14. $CH_3O + CH_4 = CH_3OH + CH_3$	65	72	49	68
15. $CH_3O + O_2 = CH_2O + HO_2$	4	21	4	17
21. $CH_3O + CH_2O = CH_3OH + CHO$	9	3	27	7
43. $CH_3O + CH_3OH = CH_3OH + CH_2OH$	12	2	10	6
Make Methyl Peroxy				
3. $CH_3 + O_2 = CH_3OO$	100	100	100	100
Destroy Methyl Peroxy				
4. $CH_3OO = CH_3 + O_2$	*	*	*	*
6. $2CH_3OO = 2CH_3O + O_2$	33	48	32	40
9. $CH_3OO + HO2 = CH_3OOH + O_2$	30	17	31	25
7. $2CH_3OO = CH_2O + CH_3OH + O_2$	14	21	13	17

TABLE 5-10 (Cont'd)

	Make Methyl Hydrogen Peroxide				
9.	$CH_3OO + HO_2 = CH_3OOH + O_2$	60	96	60	59
18.	$CH_3OO + CH_2O = CH_3OOH + CHO$	12	2	11	14
38.	$CH_3OO + CH_3OH = CH_3OOH + CH_2OH$	15	1	14	12
48.	$CH_3OO + H_2O_2 = CH_3OOH + HO_2$	10	0.4	12	7
	Destroy Methyl Hydrogen Peroxide				
28.	$CH_3OOH = CH_3O + OH$	100	100	100	100
	Make Methyl				
4.	$CH_3OO = CH_3 + O_2$	*	*	*	*
14.	$CH_3O + CH_4 = CH_3OH + CH_3$	55	50	58	55
5.	$OH + CH_4 = H_2O + CH_3$	38	43	35	38
	Destroy Methyl**				
3.	$CH_3 + O_2 = CH_3OO$	87	88	97	98

*Equations 3 and 4 represent an equilibrium favoring the formation of CH_3OO; therefore, equation 4 does not give any net formation of CH_3 or removal of CH_3OO.

**Since the equilibrium favors formation of CH_3OO, the rate of equation 3 is greater than 4 and the net rate of removal of CH_3 is equation 3 minus equation 4. This difference was used in comparing the various rates of destroying methyl.

5.3.1.2.4 Effect of Reaction Variables

Temperature, pressure, and initial reagent concentrations are adjustable parameters:

1. The effect of temperature on 3:1 methane: air is shown in Figures 5-33(a) and (b). As expected, the rate of oxidation increases with temperature. Also, selectivity to methanol goes up, especially at long residence times when reaction after oxygen depletion is allowed to occur. (At higher temperature, less peroxide builds up so the tail is less.)

2. Increasing the pressure from 615 to 1015 psi does raise the rate somewhat but has little effect on product distributions in Figures 5-33(c) and (d).

3. Figure 5-34 a, b, c, and d show how raising initial concentration of pure oxygen from 2 to 20% changes methanol selectivity from 70% down to 11-26%, depending on residence time. The time for complete consumption of oxygen increases simply because there is more to use up. Formaldehyde increases during the oxidation but, by the time all oxygen is gone, has dropped off to about the same low levels in all cases.

4. Methane-lean mixtures yield low selectivities to methanol. In Figures 5-35a and 5-35b the MeOH:CO ratio is above 1.1 at 3:1 methane:air and 430^{o}C, but goes down to about .25 when the methane is dropped to 10% by substituting nitrogen. The even lower 5% methane in oxygen in Figure 5-35c reacts very slowly to carbon oxides and water. The over-riding reason is that lowering methane allows much more hydrogen abstraction from other species, including methanol, and results finally in their complete oxidation. This is clearly illustrated in Figure 5-35d where, as methane is depleted, intermediates first grow and then drop rapidly as they in turn are oxidized.

FIGURE 5-33

EFFECT OF TEMPERATURE AND PRESSURE ON METHANOL SELECTIVITY

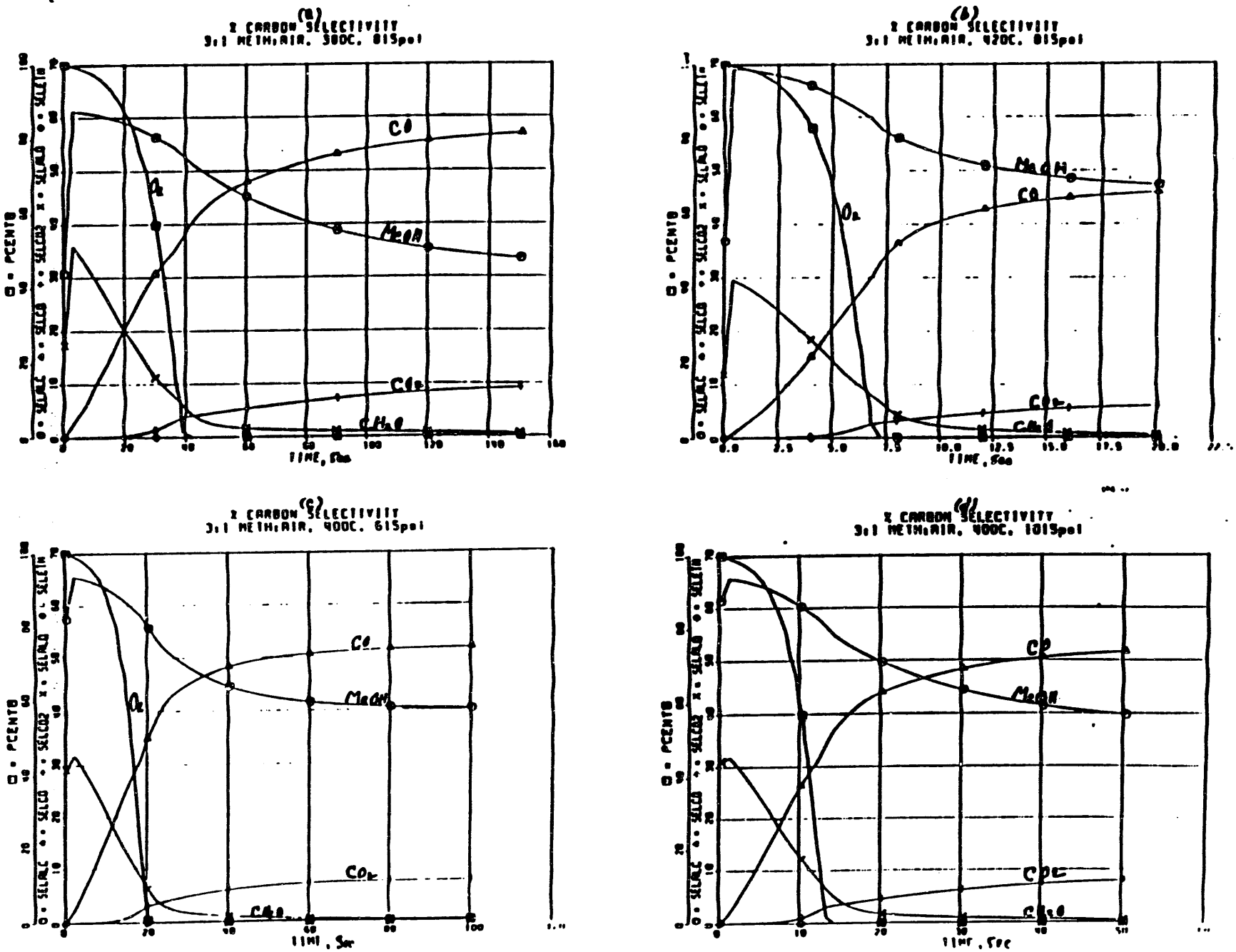

FIGURE 5-34

EFFECT OF OXYGEN PRESSURE ON METHANE SELECTIVITY

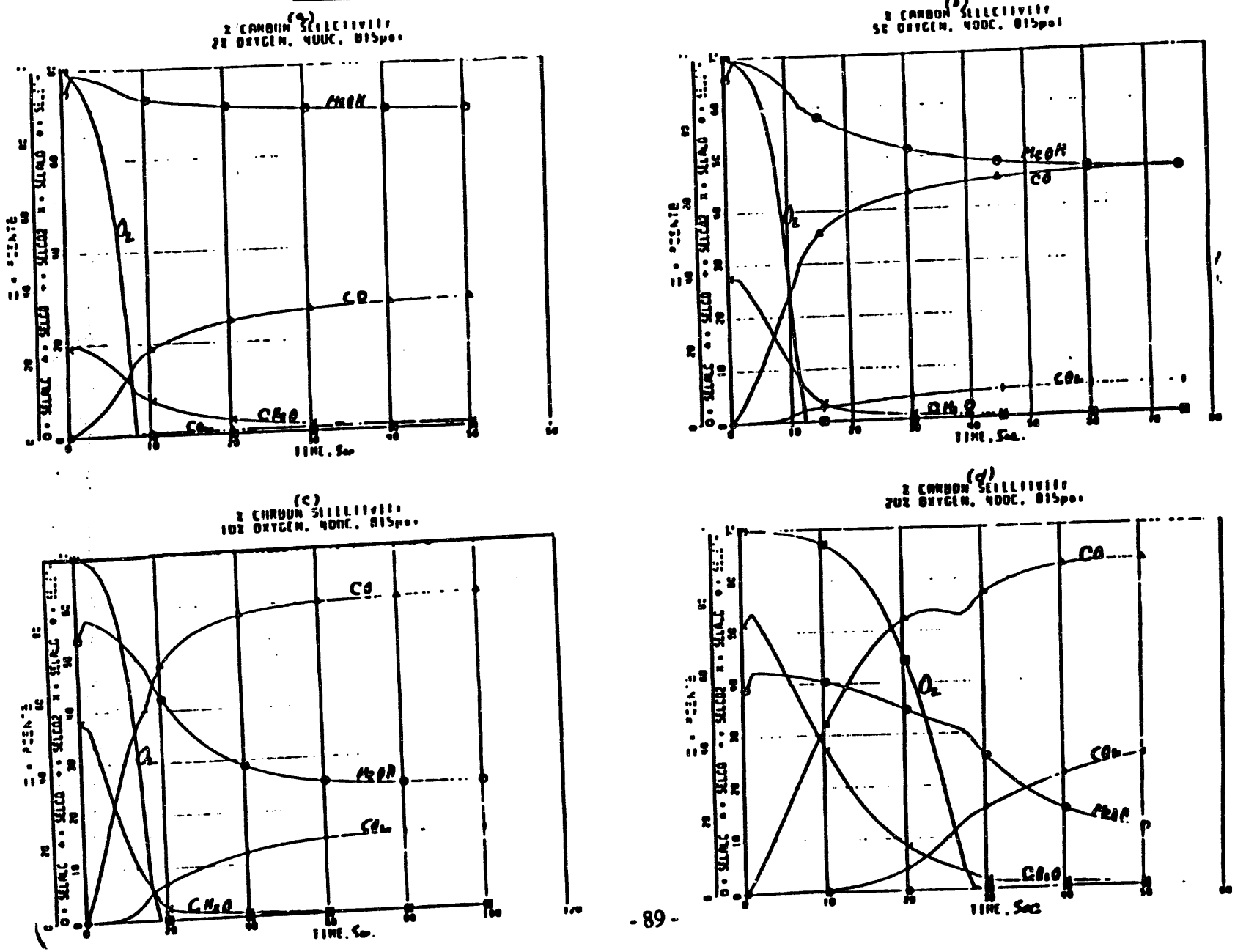

FIGURE 5-35

EFFECT OF LOW METHANE CONCENTRATION ON METHANE SELECTIVITY

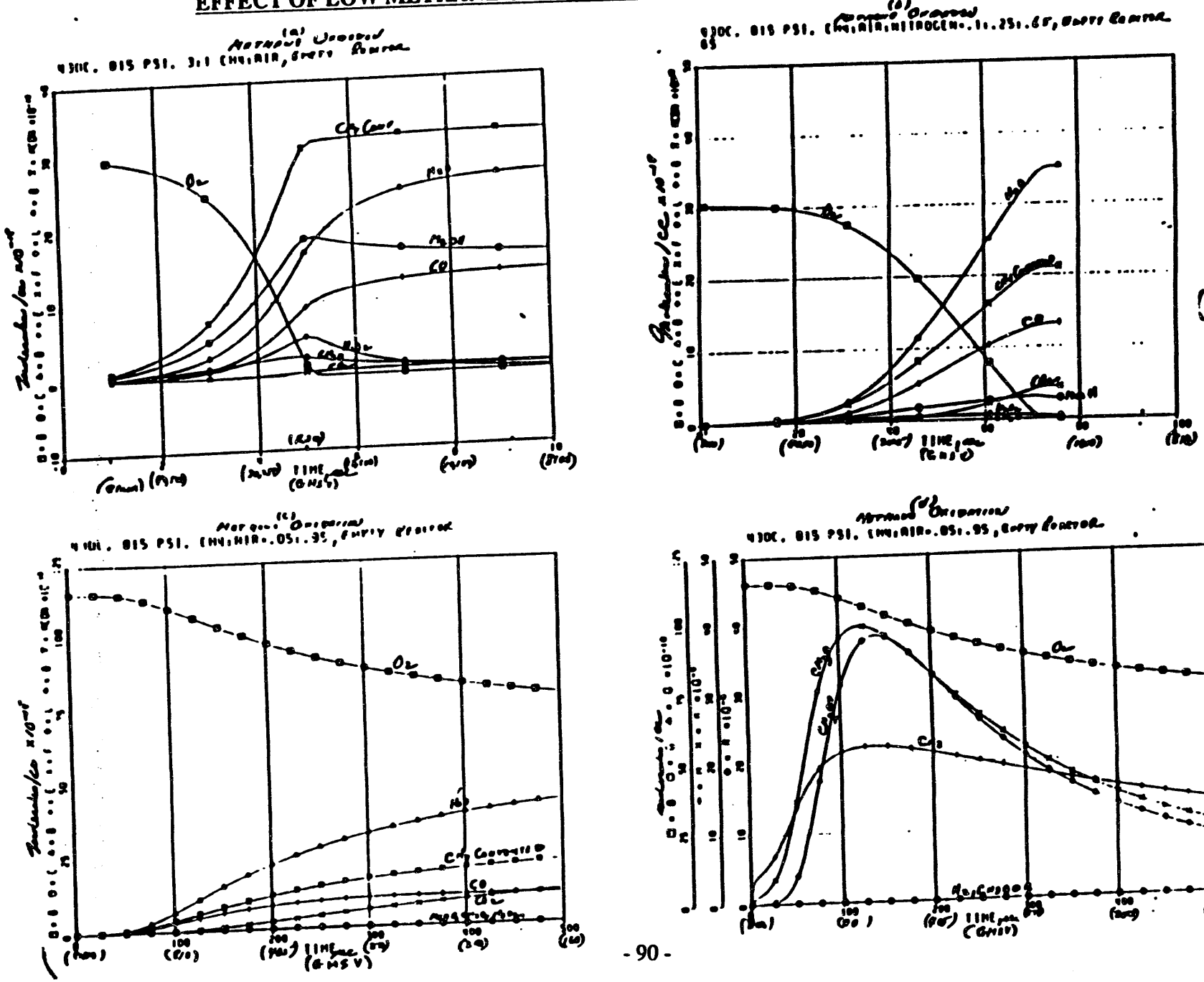

5.3.1.2.5 Inhibition by Solid

A unique feature of the Bedeneev et. al. model is inclusion of equations 56-61 to adjust for quartz surface. In U.S. Patent 4,918,249 to Sun, we report some data for oxidation of methane over glass beads. We modified the Russian reactions to make oxidized products shown in Table 5-11a and used proportionality constants to adjust an inhibition rate constant Z which in turn, was adjusted so that oxygen was consumed in the same time as the experiment. Matching experimental and calculated ratios of CO_2:CO yielded a value of 56:44. Table 5-11b summarizes these numbers and shows the averaging of the preexponential factors to give the final expression: Z = 9.8E13 exp(-31,600/RT). If Z is proportional to glass surface area (we used .03 m^2/gm beads in a .5 inch I.D., 10 cc reactor), this corresponds to Z=1 in an empty reactor at 313°C. Bedeneev et al used data at 341 and 313°C, so the agreement is excellent. Also, note in Table IIb that selectivity to methanol by model and experiment agree precisely at the two low oxygen conversions but not at the two higher.

If inhibition is proportional to surface area, one can calculate the effect of a high-surface solid catalyst (assuming the same reactivity as glass surface). Inhibition by methyl has little effect and can be ignored in our system. But, in Table 5-11c, even a 1 m^2/gm solid quenches the reaction completely. On closer scrutiny, the culprit is the MeOOH (and MeOO•). Either the Russian rate constants for destruction of MeOO are too high or the peroxide is broken into radicals which continue the chain. HOOH and HOO• removal slows the reaction at 100 m^2/gm, so that the oxidation proceeds only to 97% oxygen consumed and then levels off. Destruction by a surface prevents build-up of peroxide and thus eliminates the post-oxygen reaction 'tail' and the accompanying drop in methanol yield.

TABLE 5-11(a)

Modified Solid Reactions
Assume all adsorbed carbon goes to carbon oxides.
Y=fraction of adsorbed carbon to CO_2.

	Reaction	Rate Constant
56.	$CH_3 + (1.25 + .5Y)O_2 = 1.5H_2O + YCO_2 + (1-Y)CO.$	.005Z
57.	$CH_3OO + (.25 + .5Y)O_2 = 1.5H_2O + YCO_2 + (1-Y)CO.$	.005Z
58.	$HO_2 = .5H_2O + .75O_2.$	.005Z
59.	$CH_3OOH + (.5 + .5Y)O_2 = 2H_2O + YCO_2 + (1-Y)CO.$	.005Z
60.	$H_2O_2 = H_2O + .5O_2.$	.0015Z
61.	$H_2O_2 = H_2O + .5O_2.$	.0015Z

TABLE 5-11(b)

Calculation of the Preexponential Factor of Z
3:1 Methane:Air, 815 psi

Run	T,C	Time Sec	% O_2 Conv	Calc* Z	Alc Sel Exp	Alc Sel Calc	CO_2/CO* Exp	CO_2/CO* Calc	Preexp Factor
29	407	39.2	7	6802	47	46	1.0	.45	9.7xE13
31	418	38.6	11	10700	44	45	.61	.45	10.5xE13
32	422	38.4	26	10721	56	46	.35	.32	9.2xE13
33	430	37.9	38	14946	56	44	.29	.33	9.9xE13
								Average	9.8xE13

*Z calculated by matching the model reaction time to that seen experimentally (US patent 4,918,249). Plotting log Z versus 1/T gives $E_{act.}$ = 31.6 kcal. Forcing a match of experimental versus calculated CO_2:CO ratios gives a value of 56:44.

TABLE 5-11(c)

High Surface Area Silica
3:1 Methane:Air, 440 C, 815 psi

SA, m^2/gm	0	1	1	100
Quench COO		Yes	No	No
Seconds	4.0	N.R.	15	29
GHSV	2E4		5E3	3E3
%O left	None		None	3**
Sel, %Alc	52.7		51.6	53.1
CO	38.5		38.3	34.5
CO_2	2.2		2.0	1.0
Formald	6.4		8.1	11.4
Meth Conv	7.2		7.4	7.5

**At the end of reaction time, oxygen levels off and oxidation stops.

This brings up a problem with using a single model to predict catalyzed reactions. Generally, catalysts are high surface area solids supporting transition metals, like iron, which are known to be very active peroxide decomposers, perhaps a million times more potent than silica, and should quench the homogeneous oxidation completely. Since methane is oxidized, either the peroxide is broken into radicals which are emitted into the vapor phase, or the catalyzed oxidation occurs completely on the surface.

5.3.1.2.6 Decomposition of Methanol

The decomposition of methanol to CO and H_2 is catalyzed by some metals, for example copper, particularly under reducing conditions. As expected, the model shows a large increase in hydrogen when this reaction becomes important. Also, methanol should continue to drop at longer residence times. This reaction is not a part of the model at this time.

5.3.1.2.7 Catalysis of Methyl Radicals

One way to catalyze oxidation of methane to methanol is to create methyl radicals on a solid surface and eject them into the vapor phase. Such a situation can be modelled by adding the catalytic reaction and adjusting its rate constant. As the reaction, we chose:

$$CH_4 + .25\ O_2 = CH_3 + .5\ H_2O.$$

A careful check of all species in reaction of 3:1 methane:air at 400°C showed that a moderate quantity level of catalysis has no effect on most of them. Methanol: CO ratio goes up a little, methyl peroxide increases while hydrogen peroxide goes down, and CHO becomes more favored. Overall, however, the oxidation looks much the same, except for the expected rate increase.

Next, the rate constant was increased gradually to a very high value, with the results listed in Table 5-12a and pictured in Figure 5-36. The carbon oxides decrease while methanol goes through a maximum. Formaldehyde goes up gradually at first and then jumps to become the major product. Finally, as more of the oxygen is used up by the catalytic reaction, ethane becomes the major product. The numbers in parentheses at the bottom of the graph are the fraction of methyls supplied by the catalyst, indicating that, at the large rate constant, very few are being made in the vapor phase. Raising the temperature gives much the same overall picture, except that the rate constant does not have to be so large to make maximum methanol. Changing the catalytic reaction to produce methyl and hydroxyl radicals has only minor effect on product distributions.

FIGURE 5-36

METHANE OXIDATION

CATALYZED $CH_4 + 1/4\ O_2 \rightarrow CH_3 + 1/2\ H_2O$

815 psi, M: AIR = 3:1, 400° C

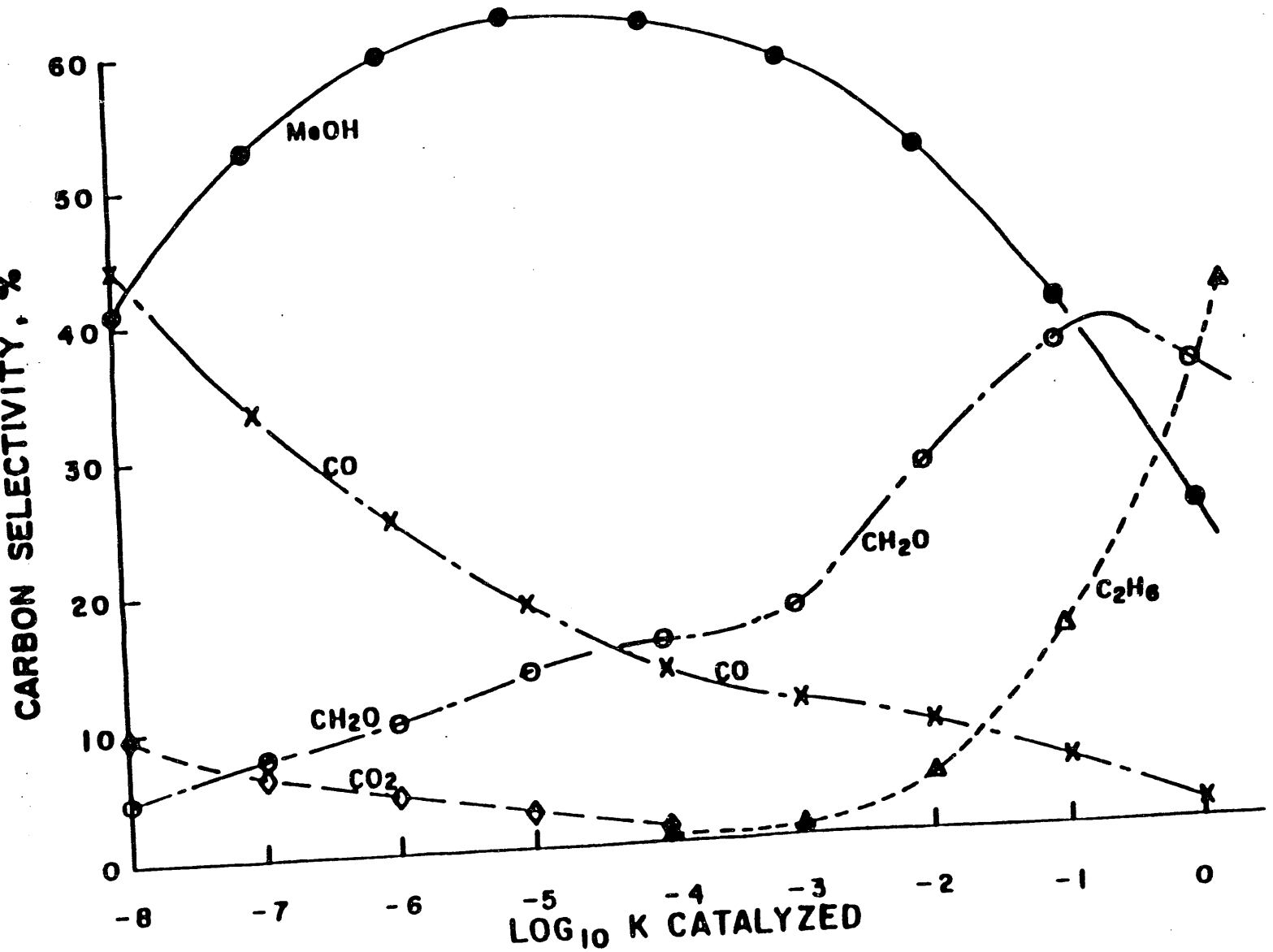

TABLE 5-12(a)

Catalyzed $CH_4 + .25\ O_2 = CH_3 + .5\ H_2O$
815 psi, M:Air = 3:1, Complete Conv. of O_2, Packed Bed, SA=.03, 400C

K Catal	E-8	E-7	E-6	E-5	E-4	E-3	E-2	E-1	1
Seconds	26	4.4	.6	.08	.01	.001	2E-4	2E-5	3E-6
GHSV	3100	2E4	13E4	1E6	8E6	8E7	4E8	4E9	3E10
Select, %									
MeOH	44.1	52.8	59.0	61.8	60.4	57.9	50.7	39.3	23.6
CO	41.5	32.9	25.6	18.3	12.9	10.4	8.5	4.9	1.7
CO_2	9.3	6.6	4.8	3.2	1.0	0.3	.08	.02	.002
Formal	5.0	7.6	10.4	13.6	15.2	19.4	28.2	36.3	33.9
C_2H_6		.01	.15	.07	0.4	.09	4.0	15.0	39.3
Meth Conv		7.3	8.0	8.4	9.0	9.1	9.2	9.8	11.8
% Me Cat.(Av)		35	43	46	65	72	82	90	

TABLE 5-12(b)

Conditions for Maximizing Methanol
815 psi, Complete Oxygen Conversion, Packed Bed (SA=.03)

Temp, C	400	400	400	400	440	440	440	440
Oxidant	.25air	.25air	.05 O_2	.10 O_2	.25air	.25air	.05 O_2	.10 O_2
Catalyze	Me	Me&OH	Me	Me	Me	Me&OH	Me	Me
K Catal	E-5	E-10	E-5	E-5	E-4	E-10	E-5	E-4
GHSV	1E6	1E6	15E5	81E4	96E5	16E5	17E5	69E5
Select, %								
Alc	61.8	59.5	64.3	55.9	67.0	68.5	69.6	62.4
Ald	13.6	12.7	13.7	12.1	14.6	12.7	13.0	14.1
Meth Conv	8.4	8.0	6.9	12.1	9.4	9.0	7.4	14.4

TABLE 5-12(c)

Methane-Oxygen Mixtures
Catalyzed $CH_4 + .25\ O_2 = CH_3 + .5\ H_2O$
Max. Methanol, Comp. Conv. O_2, 440 C (S.A.=0)

P, atm	55	30	30	30	15
% Oxygen	10	10	15	2.5	10
K Catal	E-4	E-4	E-5	E-5	E-5
GHSV	7E6	6E6	5E5	4E6	6E5
Sel, %					
Alc	62.6	62.5	57.1	78.1	62.6
CO	17.8	17.5	30.5	6.2	23.0
CO_2	2.3	2.3	1.8	.08	1.0
Ald	13.9	14.8	10.5	13.2	12.9
Meth Conv	13.6	13.6	18.3	4.12	13.9

In practice, catalyst activity would probably be adjusted to achieve maximum methanol; therefore, we settled on that point to make the variable comparisons displayed in Tables 12b and 5-12c. Methanol selectivity is favored by high temperature, low oxygen, and independent of pressure (from 15 to 55 atm). The highest methanol in these Tables is a little less than 80% at 2.5% oxygen charged -- and only 4 % methane conversion. Thus, the model predicts that our target of high selectivity at high conversions is unlikely by this type of catalysis.

5.3.1.2.8 Comparison With Reported Homogeneous Oxidations.

Among others, five groups of workers have reported work on oxidizing methane to methanol recently:

1. Gesser et al. Most of the recent reports of homogeneous oxidation of methane have come from Gesser and coworkers Pet Div Prep 36 160 (1991); App Cat 57 45 (1990); Comb Flame 79 216 (1990); and IEC Res 27 252 (1988). Their most recent results and the model agree, at least to some extent:

   a. The 1991 paper concerns the effect of reactor packing, but lists runs for empty reactor and glass beads. As Table 5-13a shows, the conversions per unit time are in good agreement. If formaldehyde is removed from the product, the model predicts somewhat less methanol in the empty reactor versus somewhat more over glass beads.

TABLE 5-13(a)

Comparison of Gesser* Data and Model
882 psi, GHSV=2200

Source	Gesser	Model	Gesser	Model
Temp, C	364	364	381	381
% Oxy Chrg	3.0	3.0	2.5	2.5
Packing	None	—	Glass	—
Res t, sec	42.3	43.4	24.9	20-25
% Oxy left	(26)	20	(0)	0
% Meth conv	2.7	2.7	3.0	3.07
Selectivity, %				
MeOH	74.7	66.0	70.0	68-66
CO	19.3	27.7	25.7	23-27
CO_2	6.3	.005	4.5	.64
Ald	--	5.81	—	8.1-6.5

*Gesser et al, Pet Div Prep 36 160(1991).

TABLE 5-13(b)

Sun Data (Gesser Apparatus) Vs Model
Charge 4.2% O_2 in Methane, 815 psi

		Selectivity, mol %				H_2:	Calculated from Model(1) Selectivity, Mol %(2)				
°C	GHSV	MeOH	CO	CO_2	Eth	MeOH	GHSV	MeOH	CO	CO_2	CH_2O
412	666	44	44	11	—	.12	1E4	59	34	1.5	5.4
411	816	49	42	9	—	.14		62	36	1.6	
412	1449	40	51	10	—	.19					
422	660	40	45	15	—	.25	E4	60	33	1.4	5.6
	to	to	to	to		to		64	35	1.5	
	6613	23	61	9	7.1	1.27					
431	533	45	42	13	—	.19	1.9E4	62	31	1.3	
	to	to	to	to		to		66	33	1.4	
	6579	23	61	8	8.2	1.29					
441	1832	43	49	8	—	.35	2.5E4	63	29	1.2	6.0
	to	to	to	to		to		67	31	1.3	
442	6679	20	63	9	9.1	1.4					
452	633	24	60	13	3.1	.80	3.8E4	65	28	1.1	6.2
	to	to	to	to	to	to		70	30	1.2	
452	6613	20	63	9	8.8	1.7					
Preheater											
500	666						666	41	39	2.0	17.52
								50	47	2.4	
								(9.0% Oxygen used)			

(1) The model always produces low ethane and hydrogen.
(2) Bold numbers calculated assuming formaldehyde is not observed.

b. In the first 1990 paper, Gesser et al report about 43 % methanol at 380-410°C and 10% oxygen at 10 atm. in an empty glass-lined reactor, stopping the reaction at "minimum" time of 160 sec on the average. Considering the difficulty in finding that minimum time, we think the model prediction, plotted in Figure 5-37 is in excellent agreement at 60 seconds and 43% methanol. (The 90% methanol from natural gas reported in the same paper is far above model predictions and must be either an experimental aberration or reflect a very beneficial "sensitizer" in the gas.)

c. The data reported in the 1988 paper are difficult to rationalize. Compared with the model, residence times used by Gesser et. al. are high by a factor of 100 or more. Many times, temperatures were so high as to give complete reaction in less than 2 seconds and tend to generate hot spots. In fact, those same workers measured temperature oscillations during reaction (first 1990 paper). Only in two cases of low oxygen at moderate temperature did the model predict about the same product distribution.

2. Work at Sun. A very thorough attempt was made to reproduce the 1988 Gesser paper in a replica of their apparatus with the yields summarized in Table 5-13(b). None of the reported high methanol yields were ever observed; in fact, methanol selectivities were generally lower than model predictions, especially at higher temperatures. Undoubtedly, oscillating reactions, back-mixing, and hot spots were occurring. Also, Sun workers saw high CO_2 and ethane, the latter at high temperatures and space velocities where hot spots are more likely.

3. Burch et. al. Their paper in J Chem Soc Far Trans 85 3561 (1989) is so constructed that insufficient input was given for us to make model comparisons, but these British workers apparently could not reproduce the Gesser 1988 yields.

FIGURE 5-37

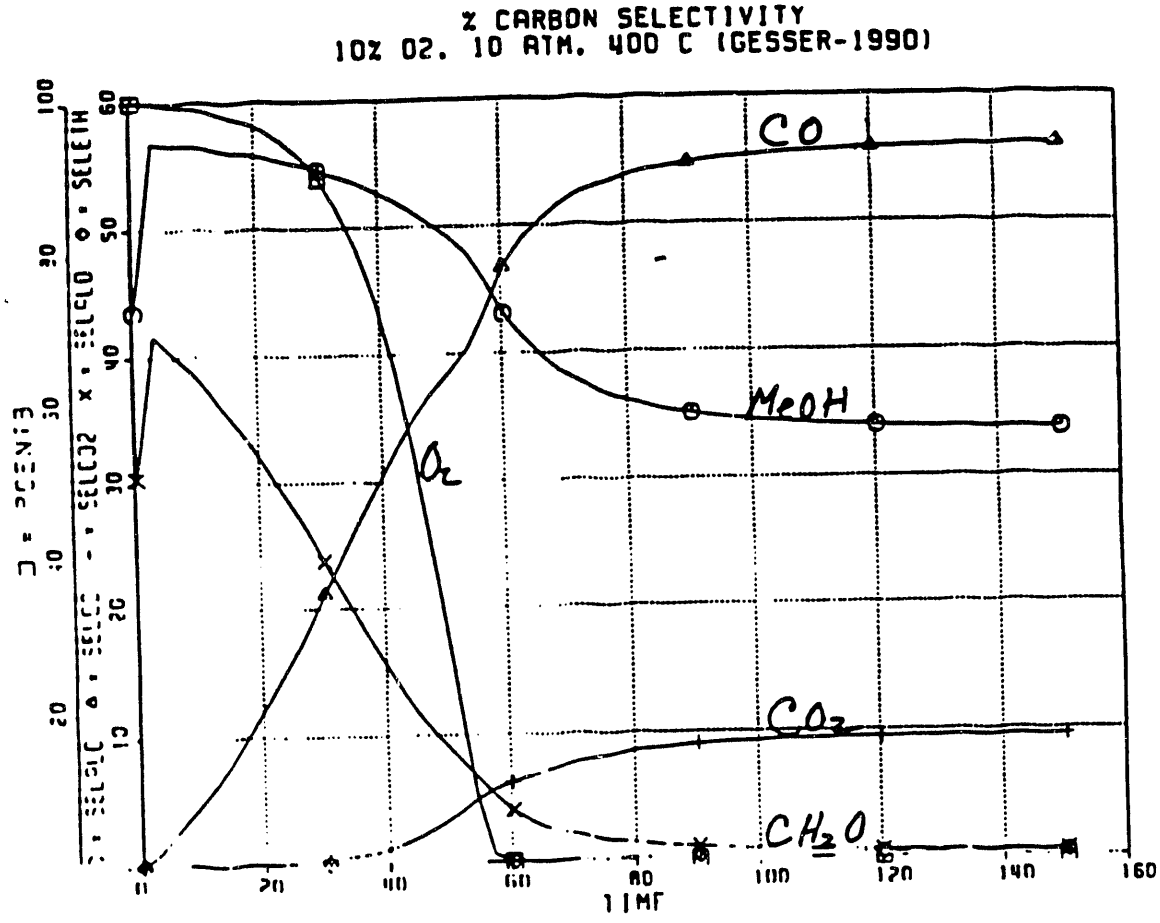
% CARBON SELECTIVITY
10% O2. 10 ATM. 400 C (GESSER-1990)
CO
MeOH
O2
CO2
CH2O
TIME

TABLE 5-14

Comparison With Rytz and Baiker(1)
450 C, 750 psi, 5% Oxygen

	Exp	Model	Exp	Model	Exp	Model
Oxygen Used	0.4	0.4	1.0	1.0	1.0	1.0
Time, sec	1.0	.76	2.51*	1.9*	3.14	4.0
Select, %						
MeOH	7.6	74.9	27.9	67.1	27.9	60.7
CO	27.6	5.7	61.3	22.9	61.3	33.2
CO_2	8.2	0	9.2	2.1	9.2	2.3
C=C	43.2	0	1.6	0	0	0
CH_2O	(10)	20.4	(0)	9.1	(0)	3.6
Meth Conv	1.71	.68	6.8	6.12	6.92	6.36

*Time when oxygen is just completely consumed.

6.0 CONCLUSIONS

We continue to make progress on tuning redox potentials of first row transition metal centers in various ligand environments to create more active catalysts for oxidatively converting light alkanes to alcohol-rich oxidates. We have been particularly successful with iron centers in increasing reduction potentials so that Fe(II) will exist in oxidizing media. It is likely that low oxidation-state iron intermediates are always available in these systems for activating the dioxygen molecule. We have been able to favorably adjust reduction potential of macrocyclic complexes by severe electron withdrawal from the macrocycle. A recent example of this is the use of the nitro group, one of the most electrophilic organic substituents, to withdraw electrons from a porphyrin macrocycle. The [redacted] Keggin ions can be varied to tune the reduction potential of iron in the framework of the polyoxometallate. The relationship between first-row transition metals and the specific zeolitic framework in which they reside can determine the predominant oxidation state of the metal and hence its ability to activate oxygen. In all of these cases, our ability to homolyze and subsequently selectively oxidize a light alkane is related to our ability to properly tune the redox chemistry at the metal center responsible for oxidation activity. We have now several families of metal catalysts capable of converting alkanes at faster rates than have ever been observed before. In some cases, such as in the oxidation of isobutane, selectivities high enough to give practical synthesis of alcohols are achieved, and in other cases, such as methanol, considerably more progress must still be made. Future work will continue to refine redox potentials for greater activity but will also concentrate on tailoring the ligand structure or metal surface specifically to enhance selectivity to desired alcohols. In this way we will ultimately have a series of catalytic agents able to selectively oxidize light alkanes to useful fuel oxygenates.

END

DATE FILMED

4/9/93